Seismic Hazard Assessment for the Geothermal Project Trias Westland at Naaldwijk, The Netherlands

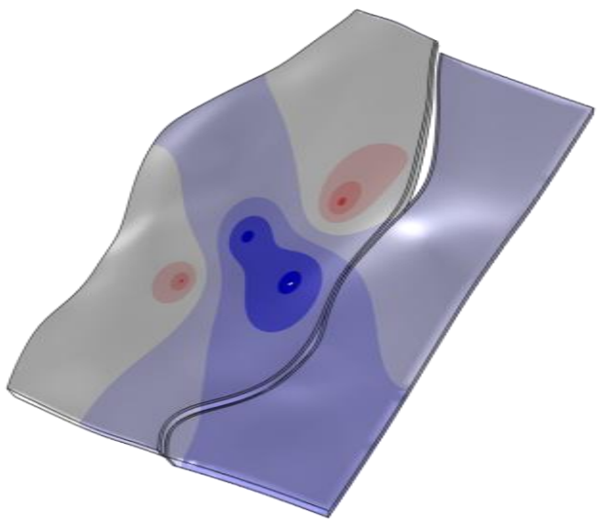

TWL001

Report title:	Seismic Hazard Assessment for the Geothermal Project Trias Westland at Naaldwijk, The Netherlands
Author(s):	[redacted], [redacted], [redacted]
Report date:	2nd September, 2019
Project:	Naaldwijk
Prepared for:	Trias Westland
Version:	190902
Archive No.:	TWL001

Contents

1 BACKGROUND

Trias Westland B.V. is planning to develop and operate a geothermal reservoir at Naaldwijk, The Netherlands. The planned system consists of two geothermal doublets targeting the Delft sandstone formation at approximately 2,300 m depth.

In the year 2018, two deep geothermal wells were drilled, forming the first geothermal doublet TWL-01. Well testing indicates that the 60 m – 80 m thick target formation exhibits a temperature of 87°C and is highly permeable (~60 Dm). Geothermal production tests with the TWL-01 doublet started in mid-July 2019 at a circulation rate of approximately 200 m^3/h. At the time of writing, the injection pressure required for geothermal circulation decreased from an initial level of 40 bar to the 30 bar level. After testing, it is planned to operate the TWL-01 doublet at 430 m^3/h.

The second geothermal doublet TWL-02 is expected to be drilled later in 2019. It is planned to operate TWL-02 with a circulation rate of 300 m^3/h. Due to their close spatial proximity with inter-well distances as small as 1.0 km, interferences between the two doublet systems cannot be excluded. Therefore, the four-well configuration is considered a single system rather than two isolated geothermal doublets.

A Quick-Scan seismic hazard assessment [1] performed for TWL-01 indicates a low to moderate induced seismicity potential [2]. With the current study, a detailed seismic hazard assessment (level 2 SHA [1]) is performed for the combined operation of TWL-01 and TWL-02.

2 MASTER SUMMARY

In the current study, the seismic hazard associated with operating the four-well TWL01-TWL02 geothermal system at Naaldwijk is investigated. The seismic hazard assessment is based on a deterministic analysis of the stress changes associated with geothermal production.

The basic geomechanical processes that could lead to induced seismicity are discussed in chapter 3 and observations from a global data set, outlining general characteristics of the induced seismicity, are presented in chapter 4. It is demonstrated that the occurrence of perceptible seismicity requires a natural, critically stressed fault in the subsurface, which is exposed to stress changes resulting from geothermal operations.

Chapter 5 summarizes the subsurface conditions at the Naaldwijk geothermal site and the previous geothermal testing operations. A local reservoir model and its numerical implementation are described in Appendix B.

The seismic hazard for a future production scenario at Naaldwijk is assessed in chapter 6. Hydraulic overpressure, mass changes, and thermal reservoir contraction (thermo-poroelastic stresses) are identified as the relevant processes causing stress changes. Using numerical simulations, it is demonstrated that the stress changes associated with a future 32 years production scenario are mainly limited to the reservoir layer. While stress changes associated with hydraulic overpressure are most relevant in the early production phase, thermo-mechanical stresses and mass changes accumulate over time. Due to the rheological behaviour of the sandstones, however, a seismic response to the stress changes at reservoir level is considered unlikely. This expectation is consistent with the absence of (measurable) seismicity in nearby hydrocarbon and geothermal reservoirs at similar depth levels.

Therefore we conclude that the occurrence of seismicity caused by geothermal production with the TWL01-TWL02 system is not expected. This conclusion is independent from potential stress interferences resulting from the ongoing production in neighboring geothermal and hydrocarbon reservoirs.

Acknowledging uncertainties of subsurface conditions, extreme scenarios are considered. If a critically stressed, seismogenic fault exists at reservoir level, the seismicity response could – under extreme circumstances - exceed the level of perceptibility due to hydraulic overpressures in the first 10 days and after 1 to 2 years of geothermal operation due to thermal cooling. To avoid the occurrence of damage relevant seismicity even under hypothetical extreme conditions, a traffic light system (TLS) is proposed for limiting the strength of earthquakes. With the proposed TLS, the remaining seismic risk associated with operating the Naaldwijk geothermal system is considered to be acceptable. It is, however, recommended to review the concept and assumptions of the current study in case a local seismic event is detected.

3 PHYSICAL MECHANISMS OF INDUCED SEISMICITY

The phenomenon of man-made seismicity is known from different energy technologies such as mining, oil and gas exploitation, water impoundment and from geothermal reservoirs [3,4]. The physical mechanisms underlying the induced seismicity are controlled by stress changes in the subsurface caused by anthropogenic activities.

If stress changes act on a pre-existing fracture or similar zone of weakness, seismicity may occur on the fracture if the ratio between shear- and effective normal stress exceeds the coefficient of friction. Let τ and σ_n denote the shear and normal stresses resolved on a fracture plane, p_{fl} the *in situ* fluid pressure, and μ the coefficient of friction, then shear slippage occurs on the fracture if [5,6]:

Equation 1: $\tau/(\sigma_n - P_{fl}) > \mu$

assuming zero cohesion.

Stress perturbations can be described by Coulomb stress changes ΔCS, which are defined as (e.g.[7])

Equation 2: $\Delta CS = \Delta\tau - \mu \cdot (\Delta\sigma_n - \Delta p_{fl})$,

reflecting the condition for criticality according to Equation 1. Positive values of Coulomb stress changes increase, negative values decrease the tendency to failure on a fault.

Mechanisms causing seismicity in geothermal reservoirs include [1,8]

- fluid pressure increase due to fluid injection,
- thermally induced stresses (thermal reservoir contraction),
- mass changes,
- poroelastic stress changes,
- and chemical processes.

All of these mechanisms may be relevant for a certain type of geothermal operation.

A necessary condition for the occurrence of induced seismicity is the existence of a (critically) pre-stressed fracture or fault, e.g. [3]. Although fractures and faults exist almost everywhere in the upper (continental) Earth's crust, different studies suggest that induced seismicity occurs predominantly in basement rock, e.g. [9–11]. A possible explanation for these observations is the different rheological behavior of the rocks. Sedimentary rocks usually exhibit a smaller shear strength compared to basement rock, e.g. [12], thus having a smaller capacity to store shear deformation energy. This could explain why critically-stressed faults are less abundant in (weak) sedimentary rocks.

The strength of an induced earthquake can be described by its seismic moment M_0:

Equation 3: $M_0 = G\ A\ d$,

where G denotes shear modulus, A is the area of the shearing plane, and d is the average slip occurring on the shearing plane. Simple mechanical considerations reveal that the shear slip displacement d cannot become arbitrary large, but is limited by (1) the capacity of the surrounding rock to absorb deformation, and (2) by the amount of shear stress driving the failure process. Therefore, the dominating parameter controlling the strength of an induced event is the area A of the associated shearing plane.

Several empirical relationships exist to convert seismic moment to earthquake magnitude. Following Hanks and Kanamori [13], we use

Equation 4: $M_w = 2/3 \cdot \log(M_0) - 6.1$

for the determination of the moment magnitude M_w. This moment magnitude scale is also used by the Royal Netherlands Meteorological Institute (KNMI), e.g. to determine earthquake strength of seismicity in the Groningen gas field. The standard magnitude scale used by KNMI, however, is a local magnitude M_L as defined in [14], and later replaced by the M_L definition in [15].

In principle, the strength of a future induced earthquake can be estimated based on the fault area on which Coulomb stress changes ΔCS cause overcritical stress conditions at a certain time in the future. This is the approach applied in chapter 6 of the current study. The approach requires an assumption on the fault’s virgin stress-strength conditions, i.e. the level of stress changes required to induce seismicity, which is generally not known. Various studies provide estimates of the stress changes that have led to observed seismicity at a certain location:

- For seismicity induced by fluid injections into the geothermal reservoir at Soultz-sous-Forêts, Baria [16] estimates that seismicity is triggered by hydraulic overpressure exceeding 3 MPa, which is consistent with numerical simulations of hydraulic overpressure in other EGS reservoirs, e.g. [17,18].
- Fluid pressure triggering threshold values as low as 0.01 MPa have been discussed in the scientific literature (see overview paper [19]). E.g., Keranen et al. [20] conclude that wastewater injection into the Arbuckle formation (Oklahoma) causes seismicity at an overpressure level as small as 0.07 MPa. Their conclusion is based on a numerical model where fluid diffusion exhibits homogeneous, three-dimensional characteristics (Figure 4 of [20]). Alternative models with a connected set of fractures, however, provide more efficient pressure propagation, resulting in a higher level of overpressure required for earthquake triggering. Using different model assumptions, Schoenball et al. [21] estimate the triggering pressure for Oklahoma seismicity to be in the order of 0.2-0.8 MPa.
- Based on a matrix-diffusion model, Husen et al. [22] estimate a level of 100 Pa fluid overpressure at which earthquakes are triggered by rainfall. Using the same data, Miller [23] estimates a triggering level in the order of 1 MPa when accounting for the strongly karstified rock.

These examples demonstrate that stress triggering levels determined from numerical models are strongly depending on model assumptions. Furthermore, it is clear that a global lower bound value for a triggering threshold cannot exist, as the lower bound value is location- and time-dependent and can become arbitrarily small during the nucleation process of tectonic earthquakes.

For a tectonically inactive area, such as the Western part of The Netherlands studied here, we assume a lower triggering threshold of $\Delta CS \geq 0.1$ MPa. We consider this assumption to be conservative in the context of the seismic hazard assessment (compare discussion in chapter 8).

4 INDUCED SEISMICITY IN GEOTHERMAL SYSTEMS

As outlined in the previous section, different mechanisms may induce seismicity[1] in geothermal reservoirs. Which of these mechanisms dominates depends on the type of geothermal operations, the timescale, the reservoir properties and the location of seismogenic faults relative to geothermal activities.

Frequently it is not possible to unambiguously relate an observed earthquake to a certain mechanism, although the location and occurrence time of an earthquake can provide constraints ruling out one or several mechanisms. For example, chemical processes are most efficient in the immediate vicinity of an injection well [24]. These cannot explain an earthquake occurring at larger distances from an injector (also compare [25]). The same is true for the mechanism of thermal cooling at an early stage of cold water injection.

Seismicity occurring in the course of hydraulic stimulations is typically interpreted as being caused by fluid overpressure reducing the effective normal stress (Equation 1) on a fault [3,9,26]. Although the current study focusses on seismicity caused by geothermal production, typical characteristics of fluid injection induced seismicity[2] can be studied using observations from hydraulic stimulations.

In granitic reservoirs, hydraulic stimulations typically produce large amounts of induced earthquakes, the largest of which exhibit magnitudes in the order of M_L=3.5 [9]. It is currently discussed if an M_w=5.4 earthquake near Pohang was triggered by geothermal stimulations [27]. In sandstone reservoirs, induced seismicity is less common and even massive hydraulic stimulations typically do not produce noticeable seismicity, e.g. [28,29].

Typical observations from hydraulic stimulations include:

- The Kaiser-Effect, implying that induced seismicity occurs only at those locations in a reservoir, where previously experienced *in situ* fluid pressures are exceeded, e.g. [30]. The Kaiser-Effect follows directly from the Mohr-Coulomb failure criterion [31].
- A systematic (temporal) increase of the maximum magnitude of the induced seismicity (Figure 1). This characteristic is a requirement for operating 'Traffic Light Systems' for risk mitigation [32,33].
- The occurrence of seismic activity after a hydraulic stimulation has been terminated (post-injection seismicity, ‘trailing effect’), with the largest magnitude event frequently occurring after shut-in [34,35]. Figure 2 shows data examples of geothermal activities and related seismicity response. In these examples, the largest trailing effect was observed after the stimulation of the DHM geothermal reservoir at Basel (Switzerland) and corresponds to a post-injection magnitude increase of 0.8 M_L magnitude units.

During geothermal production, hydraulic conditions in the subsurface may become (quasi-)

[1] Throughout this report we use the terminologies ‘induced seismicity’, ‘triggered seismicity’ and ‘caused seismicity’ interchangeably.

[2] This may also apply to re-injecting fluid during geothermal production.

stationary already at an early stage of operations, implying that the potential for inducing seismicity by hydraulic overpressure is largest at the beginning of geothermal circulation. The same holds for poro-elastic stresses, while thermo-mechanic stresses (caused by 'thermal reservoir contraction') accumulate over time [17]. After decades of operation, the thermo-mechanic stresses acting on reservoir faults can be orders of magnitude larger than poro-elastic stresses and become the dominating mechanism for inducing seismicity [36,37].

Table 1 lists earthquakes that have occurred during or shortly after mass-balanced[3] geothermal production in Europe. The largest magnitude M_L=3.5 event has occurred in a tectonically active region where the discrimination between natural and induced earthquakes may not be clear. Causality between earthquake occurrence and geothermal activities was found for the following projects, with maximum earthquake magnitude of:

M_L=2.7 at Landau [38], M_L=2.4 at Insheim [39] and M_L=2.4 at Unterhaching [40].

Although these earthquakes may be caused by different mechanisms, the current range of experience (in Europe) includes earthquakes as large as M_L=2.7 (potentially M_L=3.5) associated with geothermal production.

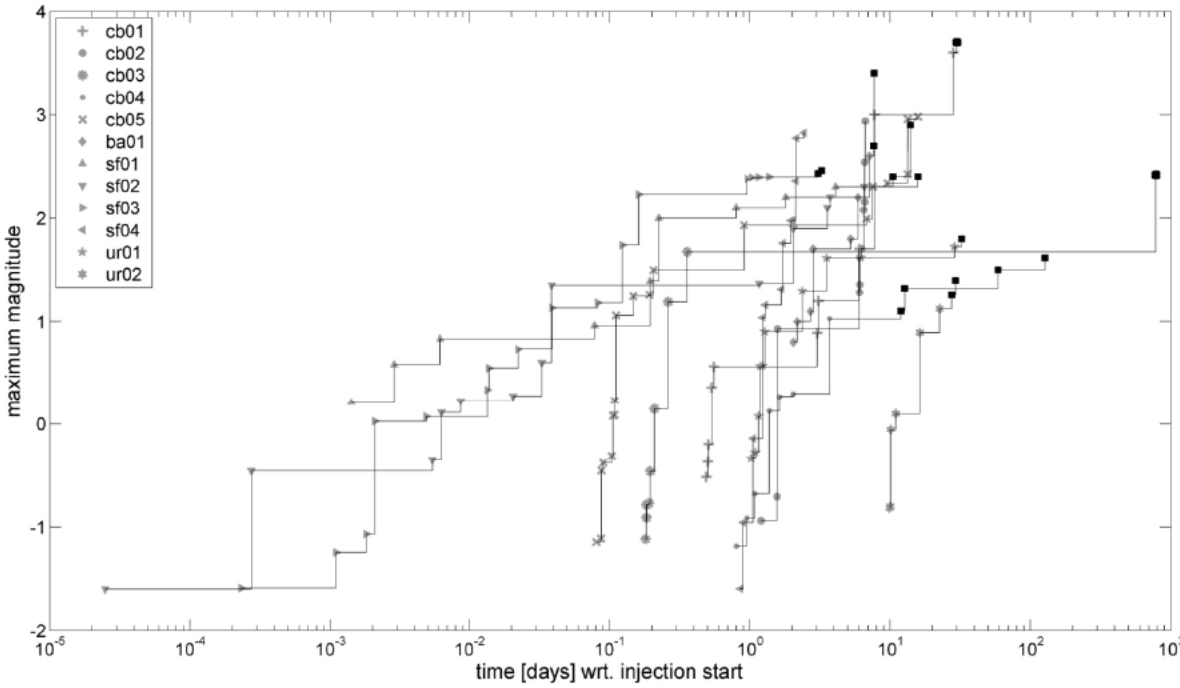

Figure 1: Maximum event magnitude as a function of injection time during hydraulic stimulation at different geothermal sites (cb Cooper Basin; ba Basel; sf Soultz-sous-Forets; ur Bad Urach). Note that data points are generated whenever previous maximum magnitudes are exceeded. Thus, a large number of data points indicate a gradual increase of the maximum event magnitude. Figure from [32].

[3] Here, mass-balanced refers to the Earth's surface, i.e. the same amount of produced fluid volume is re-injected (neglecting temperature-density effects); no assumption is made as to whether or not a closed-loop system exists in the subsurface.

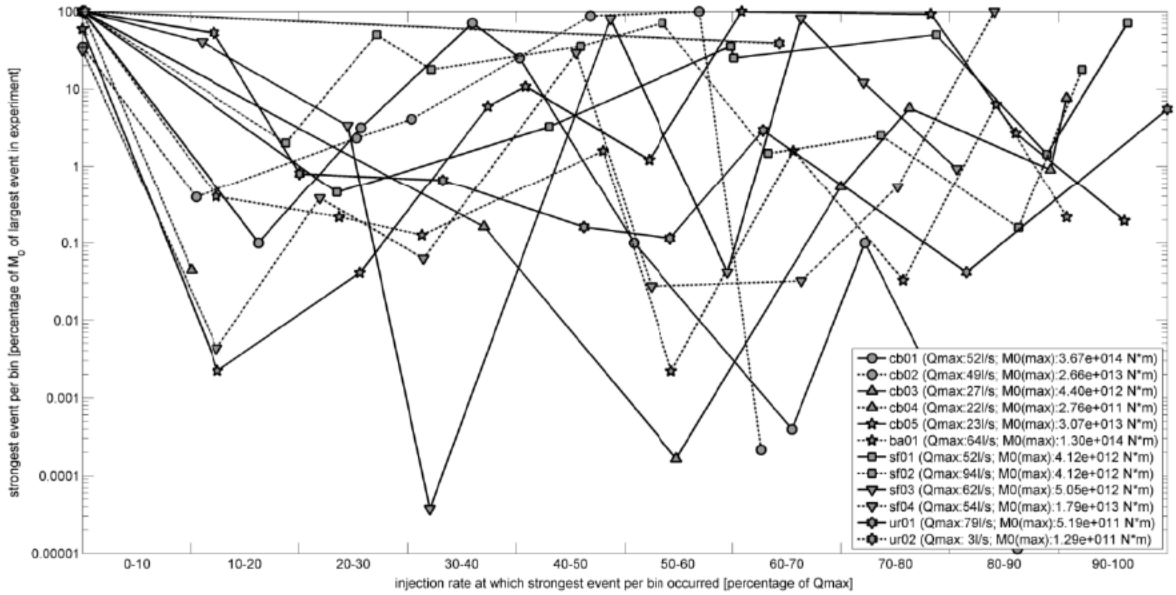

Figure 2: Normalized seismic moment release as a function of the normalized injection rate for the geothermal operations shown in Figure 1. Injection rates are binned at 10 percent intervals of the maximum injection rate operated in each experiment, which is annotated in the legend. For each bin, the earthquake with the largest seismic moment is displayed, with seismic moment stated relative to the maximum seismic moment that occurred in the experiment (listed in the legend). Note that except for cb02, cb05 and sf04, the largest seismic moment release occurred at times of 0 injection rate, i.e. during shut-in. Figure from [32].

Project	Country	M_L	Reservoir Rock
Balmatt	Belgium	2.1	carbonate
Californie	The Netherlands	1.7	carbonate
Landau	Germany	2.7	granite - sandstone - carbonate
Insheim	Germany	2.4	granite - sandstone - carbonate
Kirchstockach	Germany	0.5	carbonate
Taufkirchen	Germany	0.3	carbonate
Unterhaching	Germany	2.4	carbonate
Dürrnhaar	Germany	1.9	carbonate
Oberhaching	Germany	0.5*	carbonate
Rittershoffen	France	1.5	granite- sandstone
Lardarello-Travale	Italy	1.5	carbonate
Latera	Italy	2.9	carbonate
Monte Amiata	Italy	3.5	metamorph
Krafla	Iceland	≤ 2.0	basalt
Laugaland	Iceland	< −1	basalt
Rosemanowes	UK	2	granite
Poing	Germany	2.6	carbonate
Pullach	Germany	0.0*	carbonate
Sauerlach	Germany	1.9*	carbonate

Table 1: Largest magnitude earthquakes that have occurred during mass-balanced[4] geothermal production in Europe. Asterisk denotes earthquakes which were associated by Q-con based on spatio-temporal correlations based on earthquake catalogues and geothermal activities. Note: German carbonate reservoirs are directly overlying basement rock. Several geothermal wells intersect the basement.

[4] Here, mass-balanced refers to the Earth's surface, i.e. the same amount of produced fluid volume is re-injected (neglecting temperature-density effects); no assumption is made as to whether or not a closed-loop system exists in the subsurface.

5 PROJECT LOCATION NAALDWIJK

5.1 Geothermal Exploration Concept

The planned geothermal system consists of two geothermal doublets targeting the Delft sandstone formation at approximately 2,300 m depth (compare section 5.2). In the year 2018, two deep geothermal wells were drilled, forming the first geothermal doublet TWL-01. Well testing indicates that the 60 m – 80 m thick target formation exhibits a temperature of 87°C and is highly permeable (~60 Dm). An interference test indicates good hydraulic connectivity between the TWL-01 wells (Appendix A.2).

Geothermal production tests with the TWL-01 doublet started in mid-July 2019 at a circulation rate of approximately 200 m^3/h (Appendix A.3). At the time of writing, the injection pressure required for geothermal circulation decreased from an initial level of 40 bar to the 30 bar level. After testing, it is envisaged to operate the TWL-01 doublet at a circulation rate of 430 m^3/h.

The second geothermal doublet TWL-02 is expected to be drilled later in 2019. Figure 3 shows the location of the two doublets. Wellbore coordinates are provided in Table 2. It is envisaged to operate TWL-02 with a circulation rate of 300 m^3/h (Figure 4).

For both doublet systems the re-injection temperature will be approximately 35°C. As required by the regulating agency, geothermal production will be operated within a re-injection pressure limit of 40 bar (measured at the wellhead). At the production wells, the pressure drawdown is limited by the deployment depth of the production pumps (721 m in GT-02).

Well-testing (section A.3) indicates that hydraulic conductivity of the formation is sufficient for circulating the envisaged rate of 355 m^3/h within the 40 bar pressure limit. Recent observations, however, indicate significant near-wellbore friction losses (skin) in the injection well. These friction losses lead to a higher injection pressure (wellhead) than anticipated. The operator is currently seeking approval for increasing the injection pressure limit to 64.4 bar (wellhead) to overcome near-wellbore friction. It should be noted that an increased wellhead pressure has no impact on seismic hazard as long as the hydraulic pressure in the formation remains the same.

It is expected that approximately 1 m^3 gas (V_n) will be co-produced per cubic meter of geothermal brine. The gas will not be re-injected but used as an additional heating source.

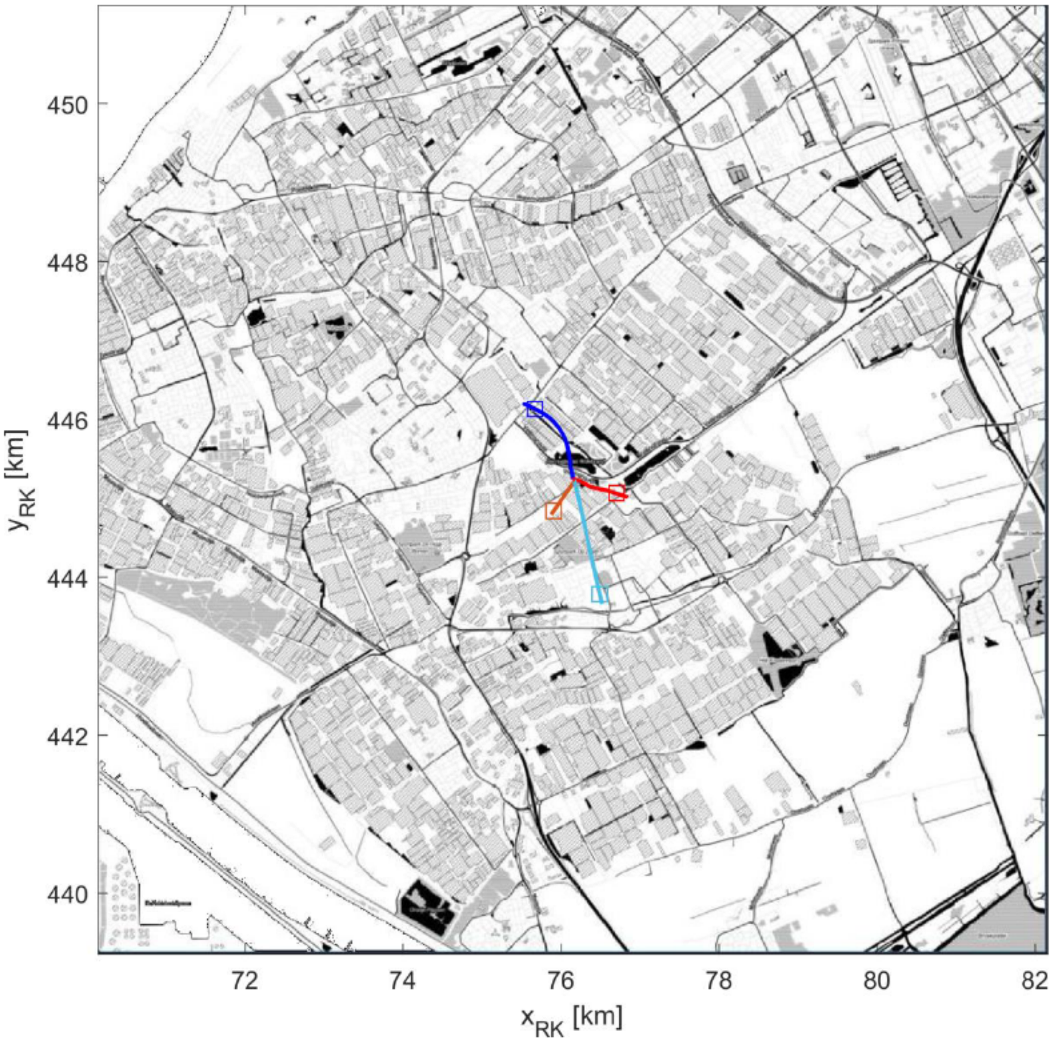

Figure 3: Wellbore trajectories of the TWL-01 (dark blue, dark red) and TWL-02 (light blue, orange) doublets. Reservoir intersections are indicated by open squares. Background map tiles by Stamen Design, under CC BY 3.0. Data by OpenStreetMap, under ODbL.

Wellbore	surface location	Top reservoir	Wellbore Bottom
GT-01	76147 / 445237 / 0	75669 / 446129 / 2313	75538 / 446192 / 3119
GT-02	76154 / 445230 / 0	76699 / 445063 / 2359	76846 / 445016 / 2526
GT-03	76169 / 445215 / 0	75908 / 444843 / 2298	75875 / 444795 / 2417
GT-04	76174 / 445210 / 0	76490 / 443785 / 2229	76518 / 443660 / 2352

Table 2: Wellbore coordinates (Easting/Northing/depth in m, Easting and Northing in RK-coordinates).

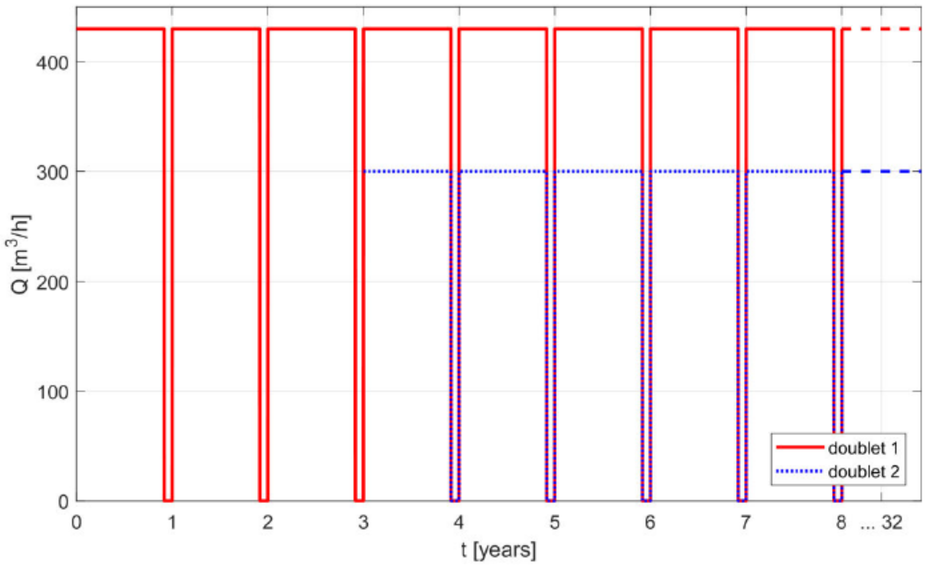

Figure 4: Envisaged production scheme for the TWL-01 (red) and the TWL-02 doublet (blue) in relative time. TWL-02 production is delayed by three years and is planned at a lower rate of 300 m³/h. It is planned to shut-down both doublets each year for a period of 30 days.

5.2 Geology

The project area is located in the south of the 'West Netherlands Basin', an approximately 60 km wide inverted rift basin in the southwest of The Netherlands and adjacent offshore area [41,42] (see Figure 5). The West Netherlands Basin experienced several phases of strong rifting during Late Jurassic - Early Cretaceous accompanied by the deposition of fluvial successions. The post-rift phase, exhibiting continued subsidence with marine transgression, was followed by a compressional phase starting in Late Cretaceous. During this phase, the basin was inverted and uplifted, which was accompanied by a reverse reactivation of the pre-existing faults [41,43].

Structurally, the West Netherlands Basin is bounded by the Mid Netherlands fault zone to the north and by the London-Brabant Massif to the south. The basin comprises several NW-SE trending structural highs and depressions divided by long NW-SE trending faults. Due to transpressional movements in the course of the inversion process, the West Netherlands Basin exhibits a series of prominent NW-SE trending flower structures [41,43].

The project area is located between two NW-SE trending major faults with a horizontal extend of approximately 10-15 km [2]. At the depth of the geothermal reservoir, the minimum distance between the mapped fault trajectory and the geothermal injection wells NLW-GT-01 and NLW-GT-04 is approximately 500 m (Figure 6).

Figure 7 shows a simplified geological profile based on the lithostratigraphic profile of well

NLW-GT-01. Tertiary and quaternary sediments with a thickness of approximately 700 m are overlaying the Mesozoic series with a total thickness of at least 3,300m. The geothermal project targets the sandstones of the Delft sandstone Member (Valanginian, Lower Cretaceous) at an expected depth of approximately 2,300 m BSL.

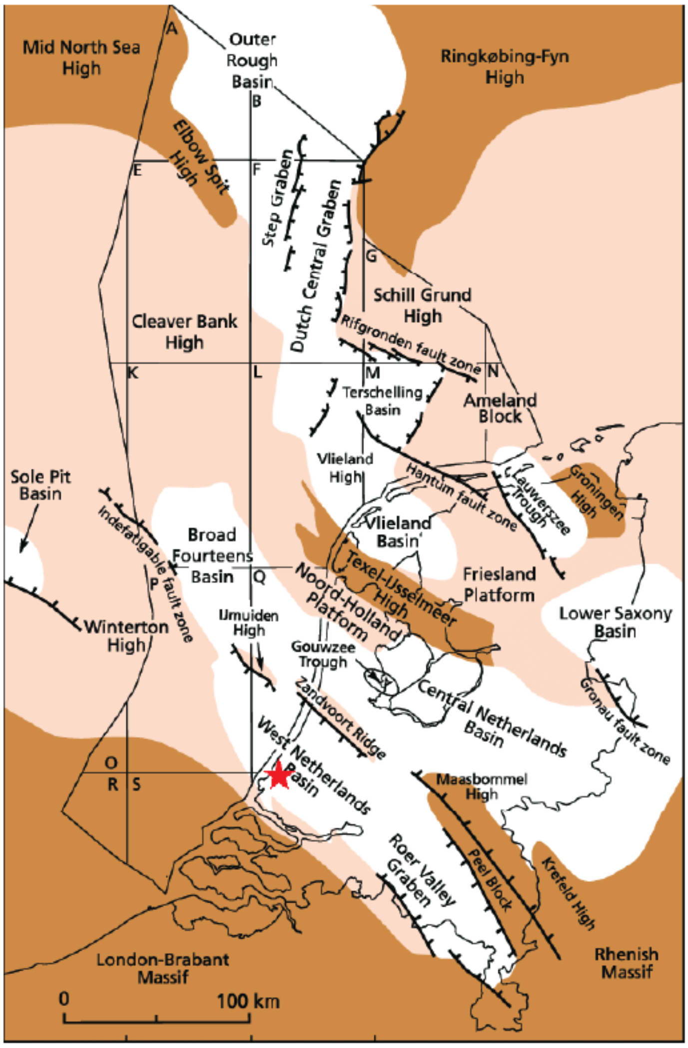

Figure 5: Map of Late Jurassic to Early Cretaceous structural elements in the Netherlands (after [44]). Figure taken from [43]. Project location is indicated by a red star.

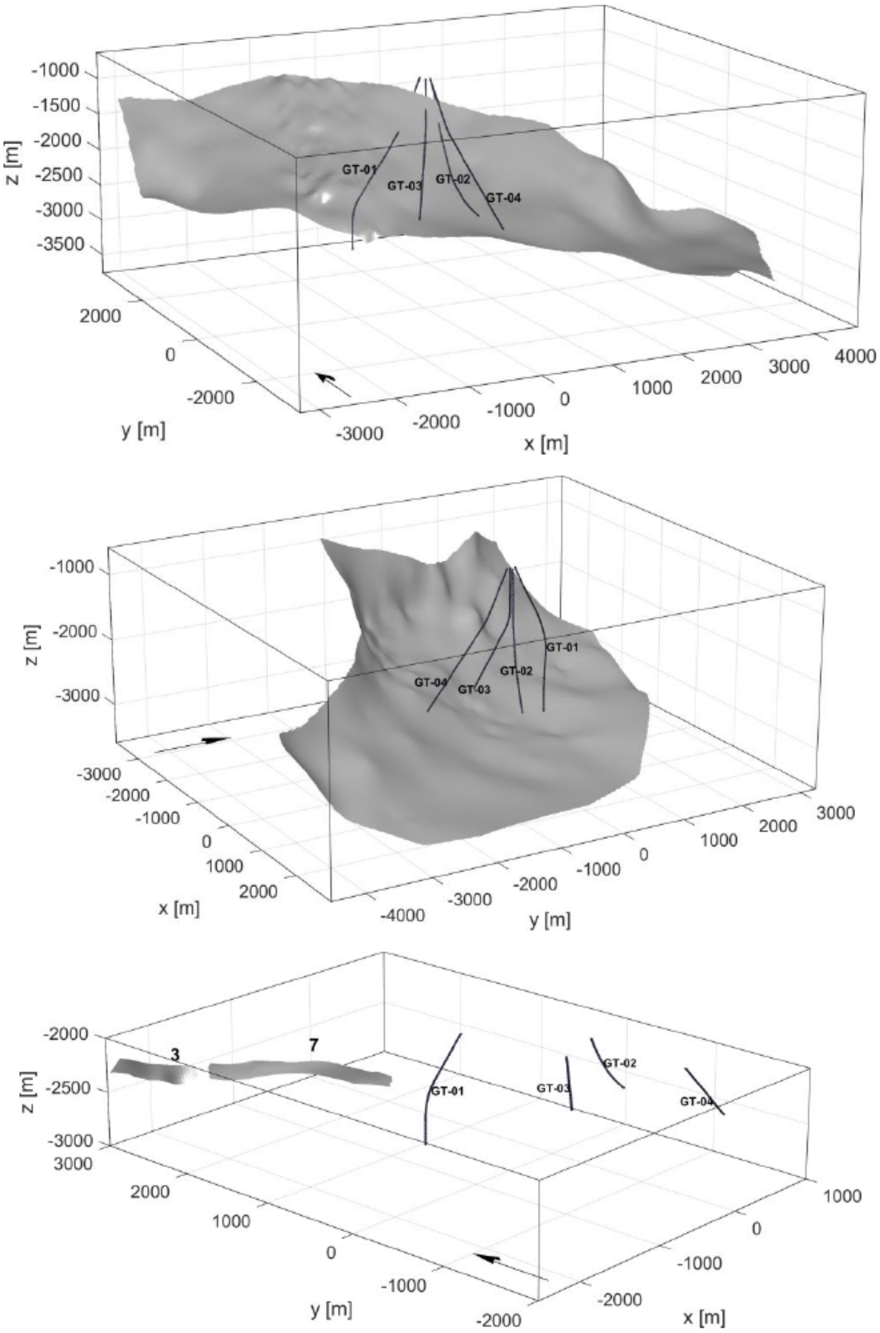

Figure 6: Local fault model derived from active seismics (data provided by HVC, June 2019). The fault model consists of boundary faults 1 (top) and 2 (center) and the smaller faults 3 & 7 (bottom) in the central reservoir block. Fault data was interpolated and triangulated with a mesh resolution of 25 m.

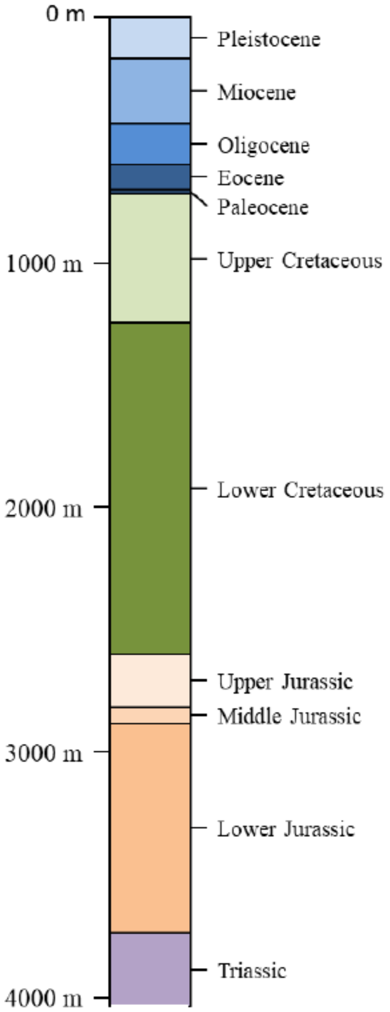

Figure 7: Simplified geological profile based on the lithostratigraphic profile of well NLW-GT-01.

5.3 Near Surface Geology

The near surface geology plays a major role for the investigation of the seismic hazard since amplitudes of seismic waves can be significantly amplified in, e.g. unconsolidated sediments. The amplification characteristics of the subsurface can be derived from the S-wave velocity of the uppermost rock layers. The lower the S-wave velocity, the larger the amplification of seismic wave amplitudes. Information on the near surface characteristics for the project location is available as a map of subsoil classes [45] (see Figure 8). The entire project region is characterized by soft soils ('slappe grond') implying a near surface S-wave velocity $V_{s30} \leq$ 200 m/s (Table 3). For the current study we assume V_{s30}=180 m/s throughout the project region.

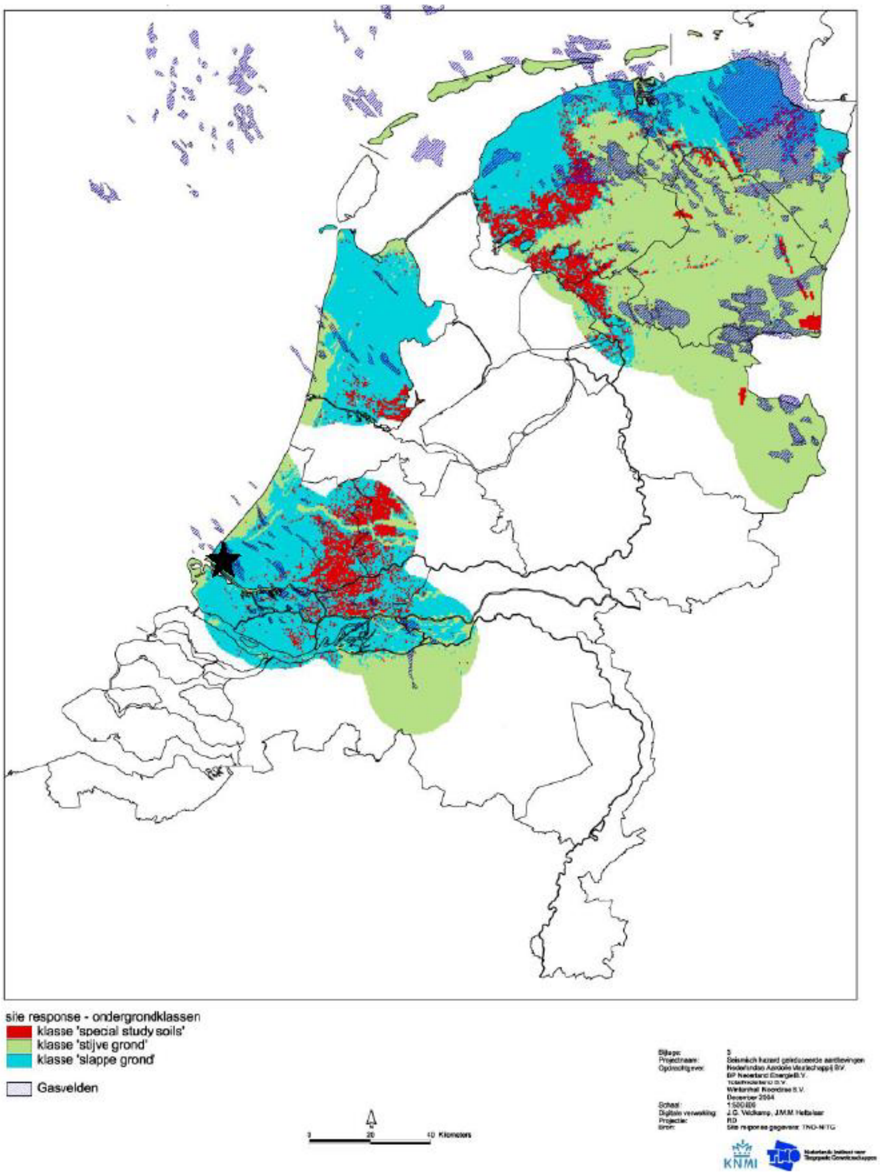

Figure 8: Map of the subsoil classes for The Netherlands. Figure taken from [45]. Project location is indicated by a black star.

subsoil class	v_{s30} [m/s]
slappe grond	≤ 200
stijve grond	> 200
special study soils	-

Table 3: Description of subsoil classes according to [45].

5.4 Stress Field

No measurements of *in situ* stresses were performed in the TWL-01 wells. From neighbouring wells, an orientation of NNE335° is obtained for S_H [2], which is in good agreement with the regional stress field orientation indicated in the World Stress Map [46].

Stress gradients in the project region are largely unknown. For the current study the possibilities of a normal-faulting as well as a strike-slip regime are considered.

It is likely that the local stress field near the geothermal reservoir has been distorted by previous production from the neighbouring oil and gas fields De Lier and Gaag as well as from two existing geothermal doublet systems. Even prior to the planned geothermal activities at Naaldwijk, subsurface stresses may exhibit lateral variations on a local scale.

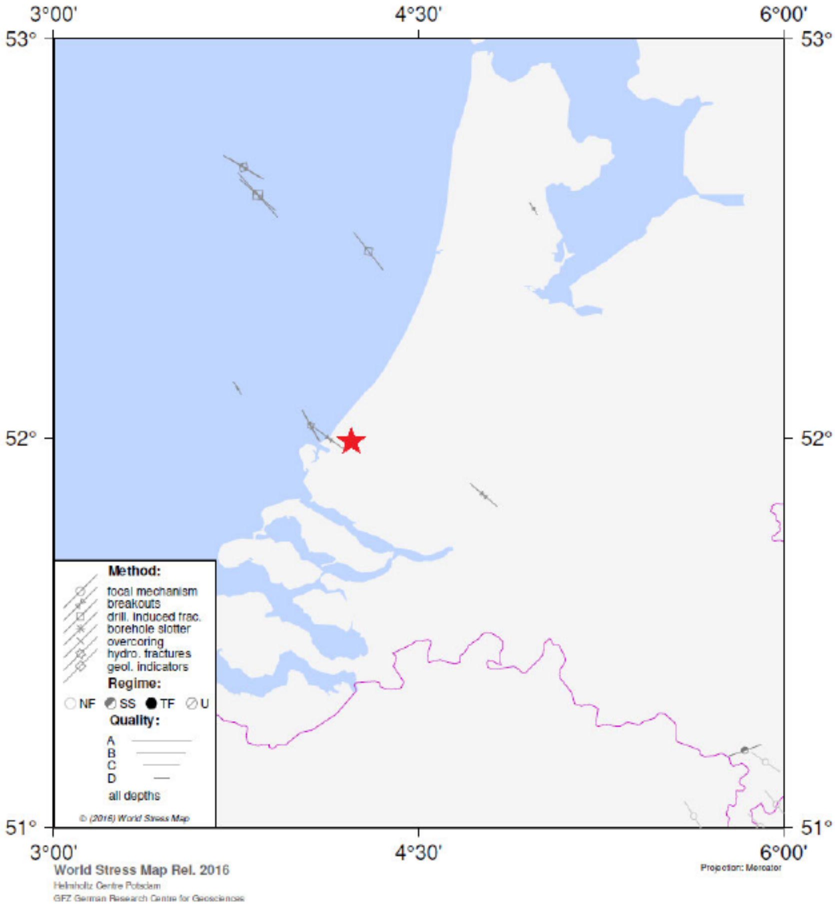

Figure 9: Map of stress field orientations for The Netherlands based on the World Stress Map [46]. Figure was generated using the onlinetool "CASMO" (http://www.world-stress-map.org/casmo). Project location is indicated by a red star.

5.5 Previous Seismicity

In the Netherlands, natural seismicity caused by tectonic processes is mainly restricted to the South-East of the country where faults are active (e.g. Roer Valley Graben with a maximum M_L=5.8 earthquake in 1992 near Roermond; [47]). Seismicity in the northern part of the country is characterized by induced earthquakes related to the exploitation of gas fields. Most prominent is the M_L=3.6 event near Huizinge from 2012 which has been related to the long term gas production from the Groningen field [48]. No seismicity has been registered in the South-Western part of The Netherlands and the closest earthquake to Naaldwijk occurred at a distance of 59 km[5] (Figure 10).

This is an astonishing observation given that a number of gasfields in the South-Western part of The Netherlands produce from the same reservoirs as the Northern gasfields, where gas production can be associated with seismicity. The exact reason for the different seismicity response to gas production is not yet understood.

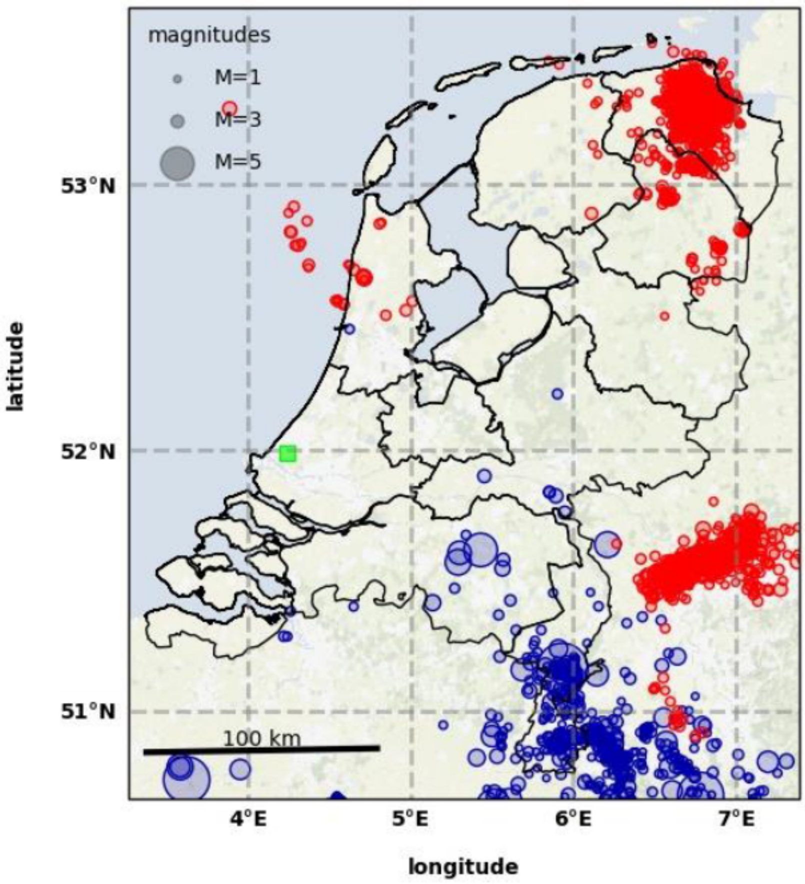

Figure 10: Seismicity distribution in the Netherlands with natural (blue) and induced (red) events displayed as circles with radius scaled according to event magnitude (basis: KNMI-catalogue as of July 2019). The project site is marked by a green square.

[5] Natural earthquake to the North-East of the site location, M=2.0, 30-1-1997.

5.6 Neighboring Geothermal Systems

Two active geothermal facilities exist in the immediate vicinity of the project site. Both systems supply heat for greenhouses and are operated in a mass balanced mode at the surface.

At a distance of 3 km to the North-West of the Naaldwijk project location, J.W.M. Scheffers / G. Verkade B.V. operate a doublet system in the Honselerdijk license field. The reservoir consists of the Delft sandstones and Pijnacker formation at a depth between 2,350 m and 2,600 m. Operational activity started in January 2014 and the maximum circulation rate was 170 m^3/hrs.

At a distance of 3.3 km to the South-East of the Naaldwijk project location, Energiewende B.V. / De Bruijn Geothermie B.V. operate a doublet in the De Lier license field. Hot water is produced from the Delft sandstones at a depth of approximately 2,500 m. Operational activity started in November 2014 (https://wellengineeringpartners.com, last visited 8.8.2019). Figure 11 shows the location of the two geothermal doublets with respect to the TWL-01 doublet.

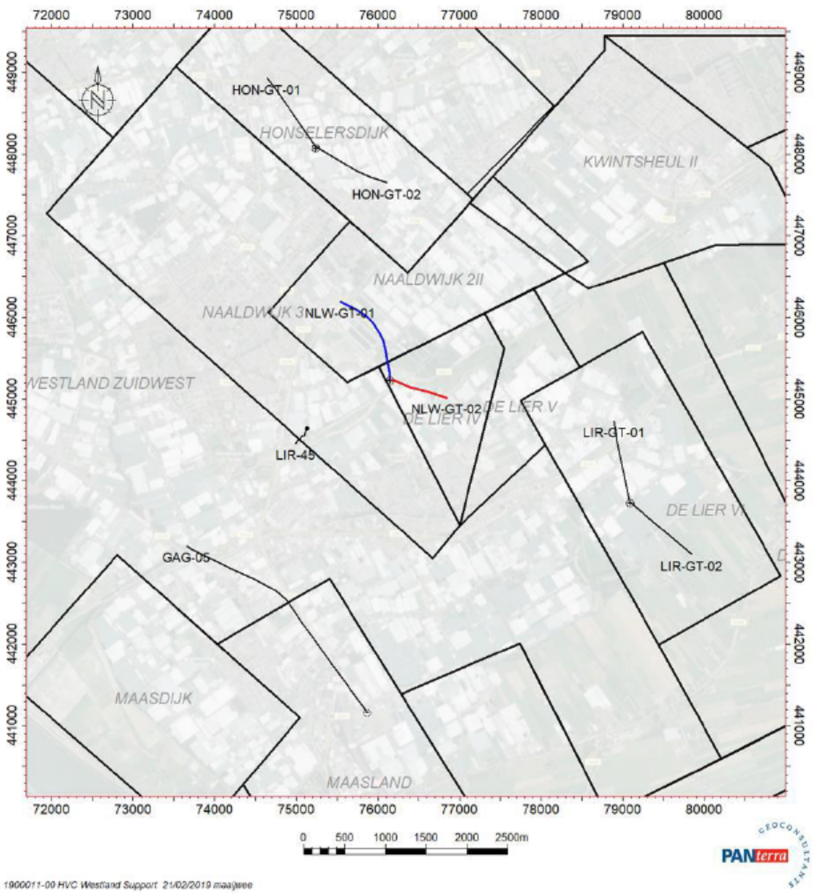

Figure 11: Geothermal facilities in the vicinity of the project location. One doublet is operated in the adjacent license field "Honselerdijk" to the North (HON-GT01/02) and another doublet in the adjacent license field "De Lier" in the South-East (LIR-GT01/02). Figure taken from [2].

5.7 Neighboring Oil & Gas Fields

Several producing oil and gas fields are located in the vicinity of the Naaldwijk geothermal location (Figure 12). Table 4 lists production data for the closest fields De Lier, Gaag, and Monster.

Oil was produced in the De Lier field between 1957 and 1993. A total volume of 2,229 million Nm^3 was extracted from a sandstone reservoir at 1,550 m depth. As a result, the reservoir pressure decreased by 145 bar from an initial pressure of 170 bar down to 25 bar. In 2013 gas production started in the De Lier field from a reservoir at 1,380 m depth. Production volumes and pressure data are not publicly available.

The Gaag field to the South and West of the project site has been operative since 1989. 7,301 million Nm^3 of gas has been extracted until 2016 from the reservoirs at a depth of 2,840 m. The reservoir consists of Rot formation, Solling formation and Main Buntsandstein. The depletion level in 2007 was 240 bar (from initially 311 bar down to 70 bar).

To the North, gas is produced in the Monster field since 1990 from the Main Buntsandstein at a depth of 2,700 m. As of 2016, a total volume of 2,650 million Nm^3 has been produced thereby decreasing the reservoir pressure from 309 bar down to less than 61 bar[6].

According to the latest Winningsplan (2017), an additional gas volume between 151-1719 million Nm^3 is expected to be produced from the Monster and Gaag fields until 2027, depending on the production scenario.

Poro-elastic stresses associated with gas production have been studied in e.g., [49]. Although their simulations focus on gas production in the Groningen field, their numerical models are to a certain extend generic and may also apply to other gas fields in The Netherlands. Based on their simulation results we expect that previous gas production from the Monster and Gaag fields has caused significant stress changes, which locally may be in the order of 1 MPa to 10 MPa on the reservoir (boundary) faults.

[6] publicly available data only until 2007

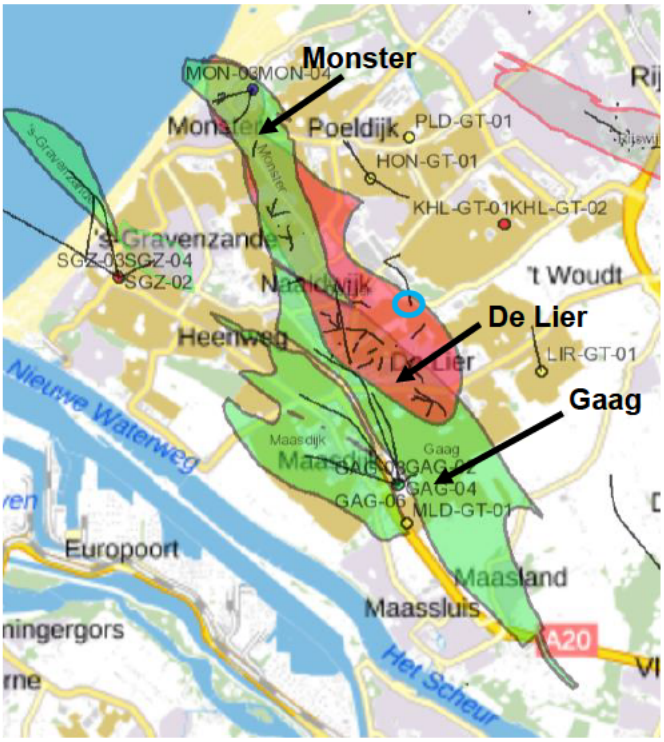

Figure 12: Location of hydrocarbon fields close to the geothermal project (blue circle). Figure from NLOG.nl with field annotations and project location added.

field name	produced volume as of 2016 [million Nm^3]	depletion as of 2007 [bar]	depth [m]	production start	status
De Lier (oil)	2,229	145	1550	1957	abandoned (1993)
De Lier (gas)	no data	no data	1380	2013	active
Gaag (gas)	7,301	240	2840	1989	active
Monster (gas)	2,650	248	2700	1990	active

Table 4: Production data for hydrocarbon fields closest to the Naaldwijk geothermal location. Data source: NLOG.nl.

6 SEISMIC HAZARD ASSESSMENT

6.1 Methodology

In general, a seismic hazard assessment is either based on a probabilistic approach, a deterministic approach, or a combination of both.

The hazard associated with natural seismicity is typically assessed by a probabilistic seismic hazard analysis, PSHA, e.g. [50,51]. The fundamental basis for a PSHA is the earthquake model, i.e. a model of the occurrence probability of a certain magnitude event in a given region and a given period of time. For natural seismicity, earthquake models are typically based on a Gutenberg-Richter type magnitude-frequency distribution. This approach assumes a stationary earthquake process, where model parameters can be calibrated by previously observed seismicity. For the current study, no such calibration data exists. A potential seismicity response to geothermal operations depends on the specific geological and tectonic conditions at Naaldwijk as well as on operational parameters. Therefore, the classical PSHA approach cannot be applied in the current context.

In principle, physics-based models could be used to numerically simulate earthquake catalogues as an input to a PSHA, e.g. [52]. Seismicity forecasts resulting from these models, however, are strongly depending on *ad hoc* parameter assumptions. Frequently, it is not even possible to predict whether or not a geothermal operation will produce any measurable seismicity at all, not to speak of any magnitude prediction [53]. Within the framework of a PSHA, this implies that hazard probabilities tend to be largely controlled by expert judgement.

To circumvent this, a deterministic approach is chosen for the current study, where the seismic hazard is assessed for hypothetical scenarios, without attempting to quantify occurrence probabilities of individual scenarios. The methodology is based on simple, physics-based models, where the potential for induced seismicity is investigated under the assumption of extreme conditions. Models include subsurface parameter combinations which are at the extreme end of previous experience, thus approximating the 'worst case scenario'. Based on theory (chapter 3) and observations (chapter 4), the models focus on re-activating a natural fault.

Acknowledging that processes may still happen outside the range of previous experience, remaining uncertainties are discussed in chapter 8.

6.2 Hazard Metric

Following the recommendations for seismic hazard assessment of geothermal systems in The Netherlands [1], we have chosen peak ground vibration (PGV) as a metric for assessing hazard. According to Dutch engineering standards [54], damage to ordinary buildings is considered to be unlikely for PGV < 5 mm/s. For vulnerable buildings, the associated vibration level is 3 mm/s. Human perceptibility is expected to start at 0.3-0.5 mm/s.

6.3 Seismogenic Processes

Basic physical considerations reveal that the seismic hazard is driven by stress perturbations related to the geothermal system in combination with the existence of seismogenic faults in the subsurface (chapter 3).

The processes that could in principle cause seismicity in geothermal reservoirs are listed in chapter 3. Most relevant for the planned operations at Naaldwijk (section 5.1) are fluid overpressure, the gradual thermal cooling of the reservoir (thermo-mechanical stresses) and mass changes. Other processes listed in chapter 3 are considered to be less relevant for the following reasons:

Given the small amplitude of hydraulic pressure perturbations with respect to total stresses, we consider the effect of **poroelastic stress changes** acting on the known faults ('expected case scenario', compare section 6.4.1) to be of secondary order compared to fluid pressure changes and thermo-mechanical stresses. This was demonstrated by generic numerical reservoir simulations [37]. Also in the hypothetical extreme case of a seismogenic (blind) fault being intersected by the injection well ('extreme scenario', section 6.4.3), poroelastic stress changes are small compared to the reduction of effective normal stress due to direct injection into the fault.

Chemical processes are typically restricted to a radius of a few meters around an injection well [24] and are thus not relevant in the current context. The same is true for the process of 'fault lubrication' as has been outlined in [25].

6.4 Geothermal Production

In the following sections we study the stress changes associated with geothermal production using numerical models as detailed in Appendix B. To keep these models computationally manageable, semi-analytical solutions are utilized for simulating thermo-mechanical stresses on the faults. Although we do not perform a fully coupled THM simulation, our simulations approximate the stress changes associated with the dominating mechanisms outlined in the previous section.

Our numerical implementation allows us to study the impact of hydraulic processes and thermo-mechanical stresses independently from each other. This has the advantage that interpretations can explicitly account for the different time-scales of these processes. For example, hydraulic processes are most relevant before the system becomes quasi-stationary while thermo-mechanical stresses accumulate over the entire lifetime of the geothermal system.

We consider different subsurface scenarios: The 'expected case', where subsurface conditions are according to the 'best of our knowledge', as well as three hypothetical extreme scenarios covering the range of possible high-risk scenarios.

6.4.1 Expected Case Scenario

The 'expected case scenario' is defined as the business case of the project developer, i.e. subsurface conditions are assumed according to exploration results (chapter 5).

The spatio-temporal evolution of hydraulic pressure was numerically simulated using the model defined in Appendix B. For these simulations it is assumed that TWL-01 is operated for 3 years at a circulation rate of of 430 m^3/h (with an annual 30 days downtime), before TWL-02 starts operating in parallel with a circulation rate of 300 m^3/h (Figure 4).

In the expected case, 1 m^3 (V_n) of gas is produced per cubic metre brine (section 5.1). Since the gas is not re-injected, the circulation is underbalanced. Assuming a typical (average) gas expansion factor of 180 to convert the produced gas volume to a net reservoir volume, we estimate that only 99.44% of the produced volume is re-injected. This is accounted for in the numerical simulations, although we notice that the impact of underbalanced operation on the spatio-temporal pressure evolution is negligible due to the assumed coupling to the far-field[7] (i.e. the constant pressure boundary to the North, Appendix B.1).

Figure 13 shows the hydraulic pressure distribution after 35 month before TWL-02 operation starts. Quasi-stationary conditions at the 0.1 MPa level were reached after approximately 60 days, i.e. the spatial extension of the 0.1 MPa isobar does not significantly change after 2 month. Operating both doublets in parallel, quasi-stationary conditions at the 0.1 MPa level are also reached after approximately 2 month following the production start of doublet TWL-02.

The hydraulic pressure distribution after operating both doublets for 32 years is shown in Figure 14. Hydraulic pressure changes on the mapped faults are generally ≤ 0.2 MPa at reservoir level. Due to the poor hydraulic conductivity of the underburden, hydraulic overpressure is negligible at basement level.

Cooling and associated reservoir contraction cause comparatively larger stress changes on the mapped faults. Figure 15 shows the simulated Coulomb stress changes on fault 1 after 8 years of operating the two doublets. Details of the numerical model are provided in Appendix B. In the sedimentary section at reservoir level, positive and negative Coulomb stress changes occur. The magnitude of stress changes increases approximately linearly with time. At those locations where positive Coulomb stress changes are concentrated, the maximum stress change is ΔCS=0.73 MPa after 8 years and further increases with time. We did not simulate Coulomb stress changes for later times as the cooling front penetrates the fault after 8 years in which case our numerical approximation of the THM solution becomes invalid. In the basement at a depth level of 4.5 km, simulated ΔCS values for boundary fault 1 are extremely small and do not exceed 1 kPa even after 32 years of operation[8].

[7] Note: the opposite scenario, where no coupling to the far-field exists, is covered by the extreme scenario investigated in section 6.4.4.
[8] For this simulation, the fault has been extrapolated to basement depth.

Coulomb stress changes on mapped faults 2 and 7 are comparatively smaller as shown in Figure 16 and Figure 17. On fault 3, Coulomb stress changes are generally smaller than 30 kPa and are thus not shown.

Neither the *in situ* stress conditions prior to operating the TWL-01 and TWL-02 doublets are known (section 5.4), nor the strength of the faults. Therefore, the simulated stress changes cannot directly be related to seismic failure. For the expected case, however, we follow the interpretation that the sedimentary section does not respond seismically to stress changes (chapter 4). We consider this to be a reasonable assumption given that the large stress perturbations associated with previous gas production (section 5.7) in the neighboring gas fields have not caused (measurable) seismicity (section 5.5).

In basement rock, where a seismic response to stress changes is considered likely, the amplitude of stress changes is negligible. Therefore we conclude that a (measurable) seismicity response in the expected case is unlikely.

We also note that the current circulation test (Appendix A.3) has not caused measurable seismicity. Using the ‘expected case’ numerical model we find that faults 1 and 7 have already been exposed to Coulomb stress changes in the order of 0.1 MPa after the first 6 days of the current circulation test.

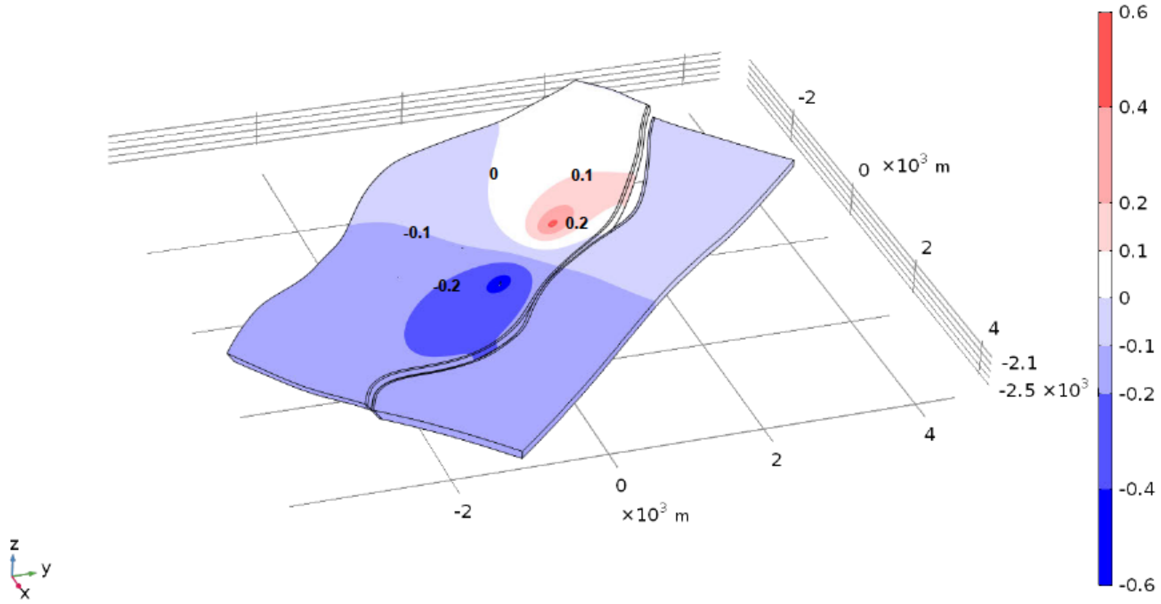

Figure 13: Spatial distribution of pressure changes after operating TWL-1 for 3 years before launching TLW-02. Pressure changes in MPa according to the colour scale with selected isobars labelled in the figure. Y-axis points to the North.

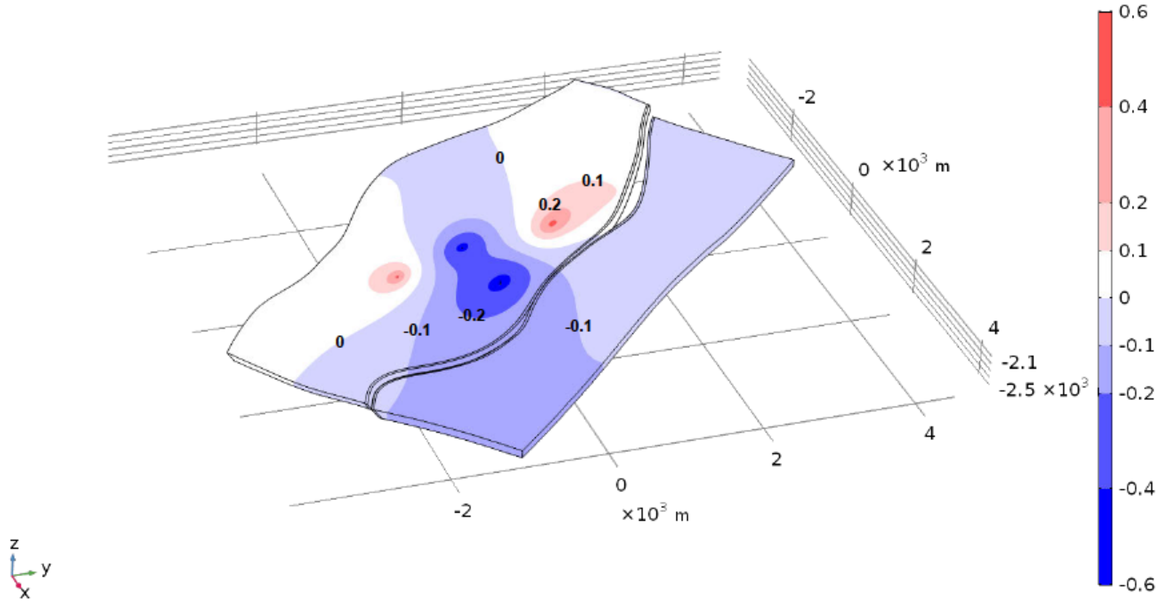

Figure 14: Spatial distribution of pressure changes after 32 years of operating TWL-1 and TWL-2 in parallel. Pressure changes in MPa according to the colour scale with selected isobars labelled in the figure. Y-axis points to the North. Note: Quasi-stationary conditions at the 0.1 MPa level were reached after approximately 2 month.

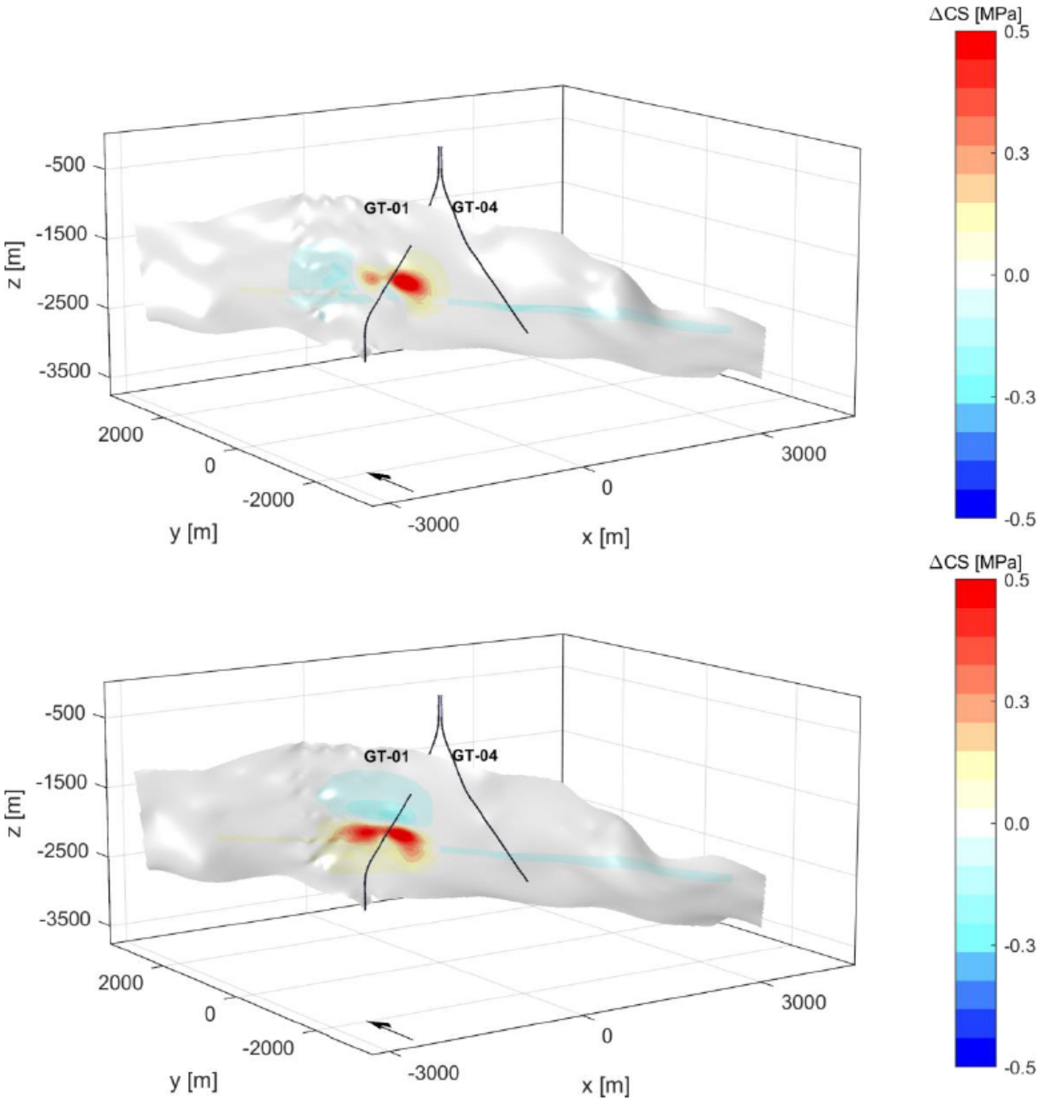

Figure 15: Simulated Coulomb stress changes ΔCS on boundary fault 1 after 8 years of operation. ΔCS in MPa according to the color scale. Stress changes for a dextral strike-slip failure mechanism (note: sinistral failure is associated with similar stress changes) is shown at the top, stress changes for a normal faulting mechanism at the bottom. Red colors indicate those regions where failure is promoted; blue colors those regions where failure is inhibited. Note: data saturated at +/- 0.5 MPa; the maximum value is 0.73 MPa.

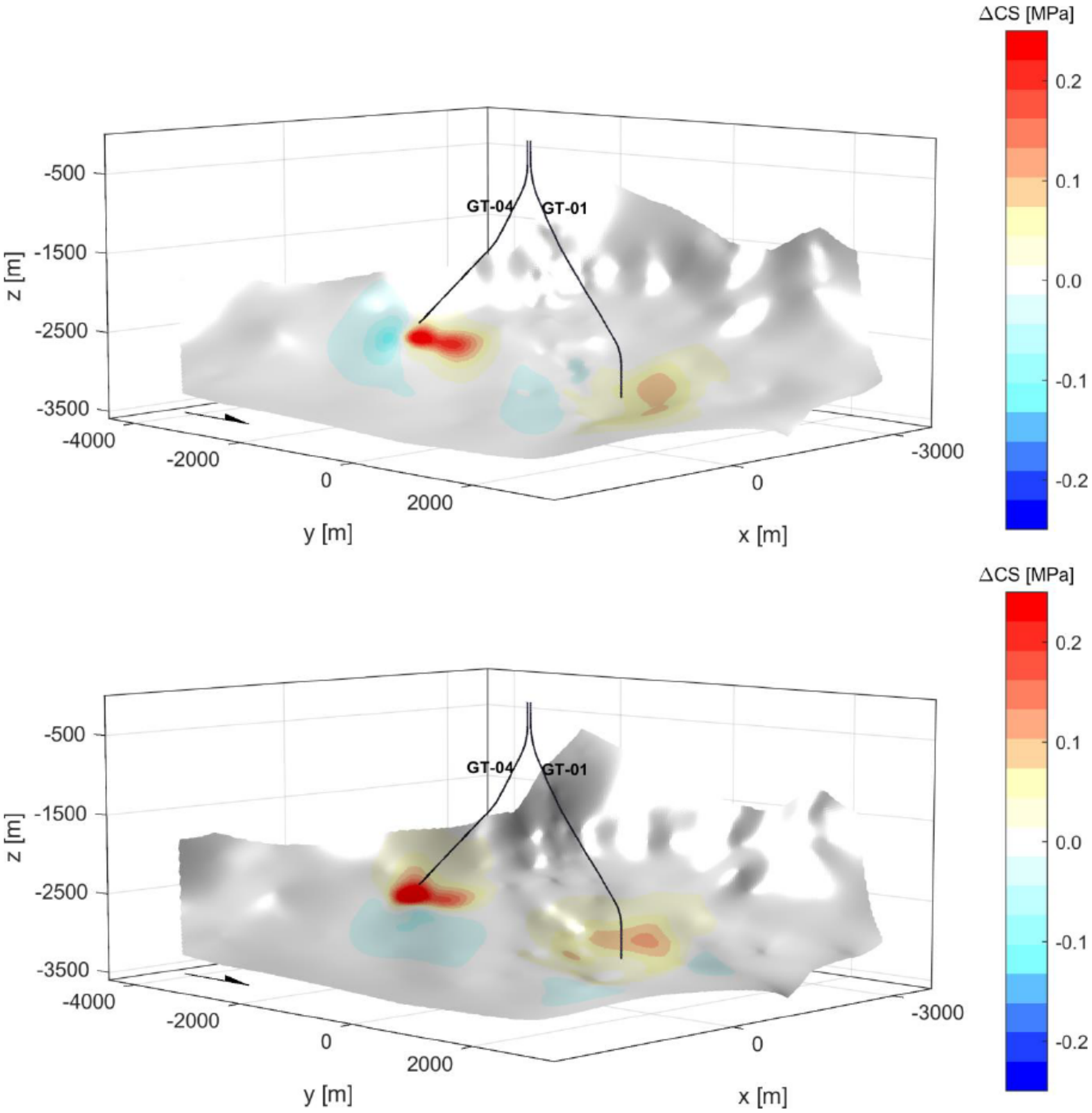

Figure 16: Simulated Coulomb stress changes ΔCS on boundary fault 2 after 8 years of operation. ΔCS in MPa according to the color scale. Stress changes for a dextral strike-slip failure mechanism (note: sinistral failure is associated with similar stress changes) is shown at the top, stress changes for a normal faulting mechanism at the bottom. Red colors indicate those regions where failure is promoted; blue colors those regions where failure is inhibited. Note: data saturated at +/- 0.25 MPa; the maximum value is 0.31 MPa.

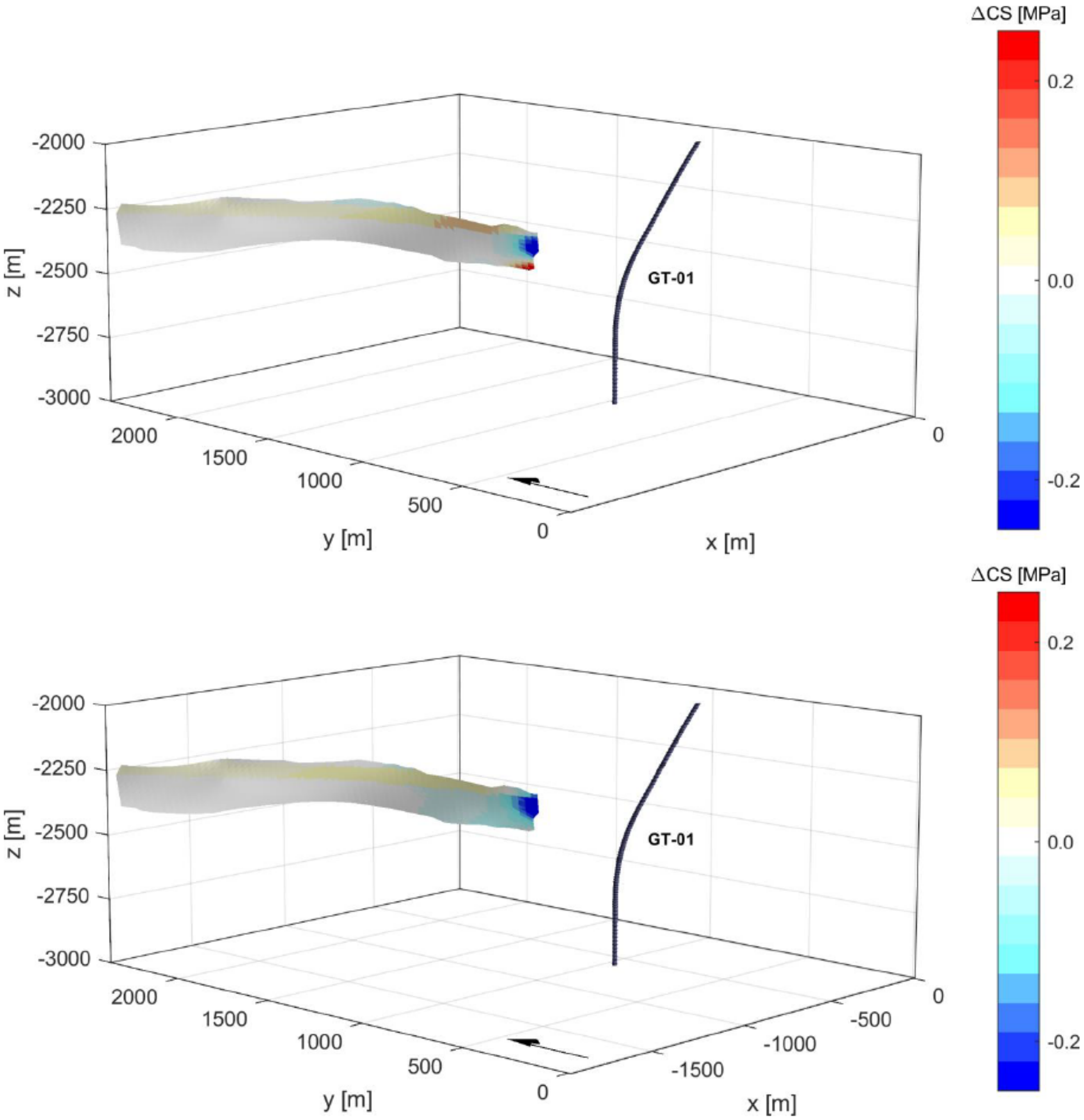

Figure 17: Simulated Coulomb stress changes ΔCS on fault 7 after 4 years of operation. ΔCS in MPa according to the color scale. Stress changes for a dextral strike-slip failure mechanism (note: sinistral failure is associated with similar stress changes) is shown at the top, stress changes for a normal faulting mechanism at the bottom. Red colors indicate those regions where failure is promoted; blue colors those regions where failure is inhibited. Note: data saturated at +/- 0.25 MPa; the maximum value is 0.28 MPa.

6.4.2 Extreme Scenario: Fault Activation at Reservoir Level

This scenario resembles the previous one, except that the sedimentary section of the faults is assumed to be critically stressed. Already smallest stress perturbations on the faults are assumed to be sufficient to initiate seismicity.

For this scenario we estimate the maximum earthquake magnitude M_{max} based on the fault area subjected to a certain level of Coulomb stress increase ΔCS, i.e. we consider the fault area exposed to a critical level of $\Delta CS \geq \Delta CS_{crit}$ while assuming that the fault is half a seismic stress drop away from criticality [55]. We consider critical levels of ΔCS_{crit} =0.1 MPa and ΔCS_{crit} =0.5 MPa, although we note that the gradual temporal evolution of M_{max} as well as its absolute level are not critically depending on a particular choice of ΔCS_{crit} (compare Figure 18).

We use the numerical model described in Appendix B to simulate ΔCS on the mapped faults. Figure 18 to Figure 20 show the temporal evolution of M_{max} on the faults[9]. Although the absolute value of M_{max} is, to some extent, depending on several parameter assumptions, the slow and gradual increase of M_{max} is independent of the assumed parameters. Therefore, the traffic light system proposed in chapter 7 is considered an effective mitigation measure.

The complex evolution of M_{max} on fault 7 (0.2 MPa stress drop model) is due to the competing impact of reservoir overpressure and thermo-mechanical stresses. In the initial circulation phase M_{max} reaches its maximum after approximately 50 hours prior to reaching quasi-stationary conditions (see inset in Figure 20). Thereafter, the impact of hydraulic overpressure is slightly reduced due to the influence of the production well. After quasi-stationary conditions are reached, thermo-mechanical stresses reduce the tendency to failure in a normal faulting regime (whilst their contribution is small in a strike slip regime). The second doublet TWL-02 is launched after three years, reducing fluid pressure on the fault as well as the corresponding maximum magnitude. With increasing time, potential maximum magnitude grows as increased thermal cooling dominates the stress perturbation on the fault.

[9] Coulomb stress changes on fault 3 (not shown) do not exceed 30 kPa and are considered negligible.

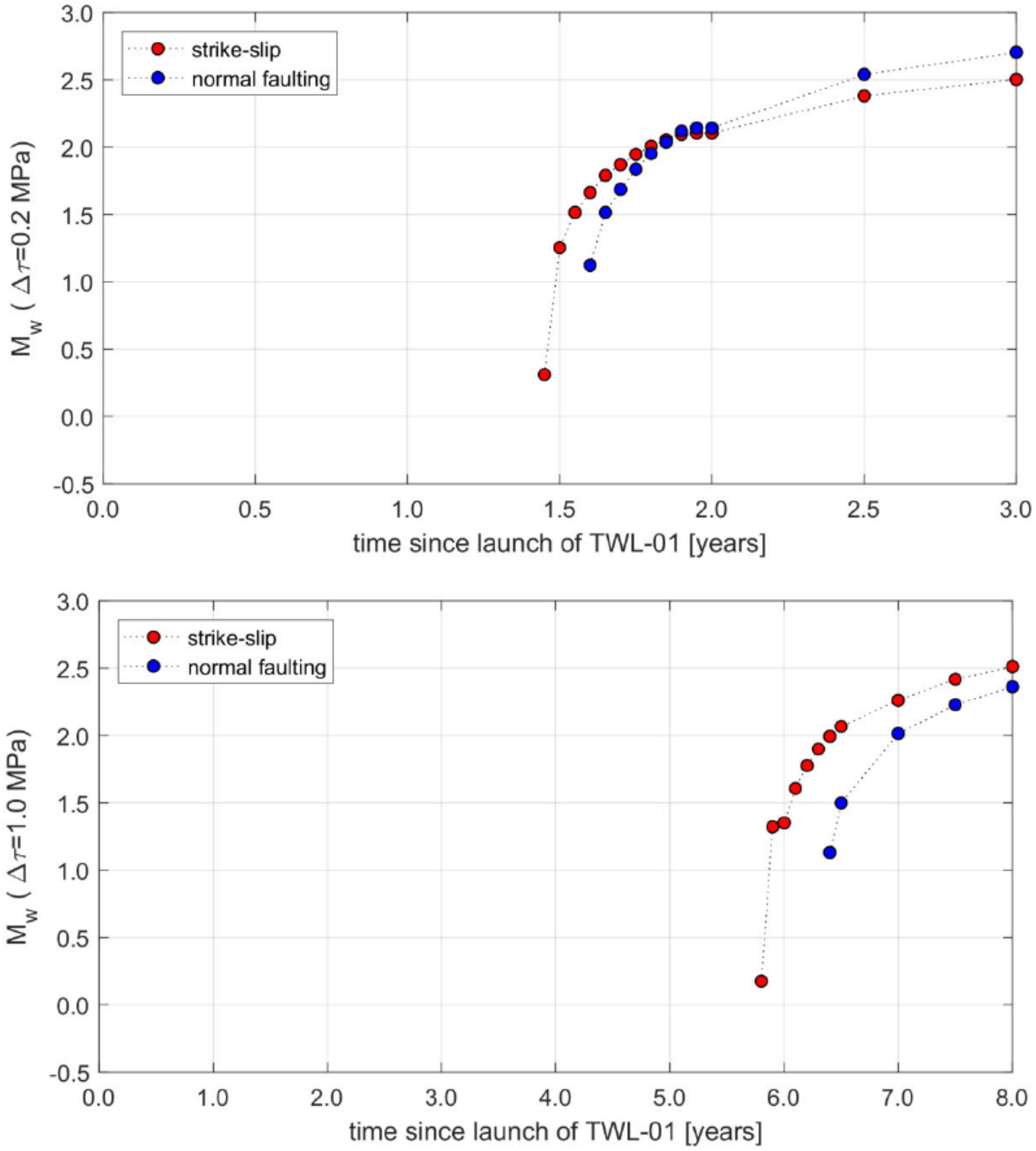

Figure 18: Simulated temporal evolution of maximum earthquake magnitude on boundary fault 1 assuming that the boundary faults react seismically at sedimentary level. A stress drop of 0.2 MPa (top) and 1 MPa (bottom) has been assumed for estimating M_{max}. Two potential failure mechanisms, strike slip or normal faulting, are considered.

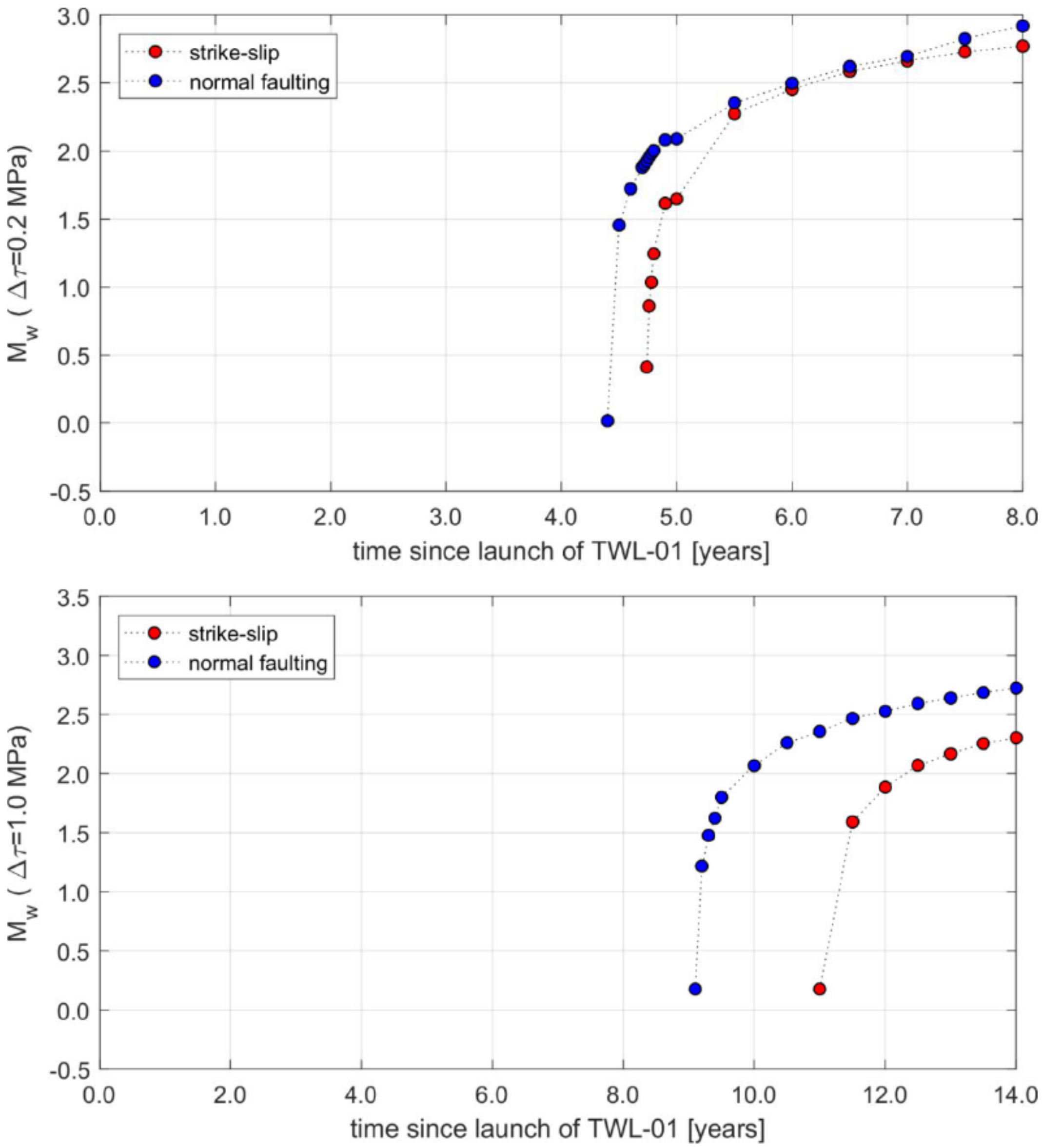

Figure 19: Simulated temporal evolution of maximum earthquake magnitude on boundary fault 2 assuming that the boundary faults react seismically at sedimentary level. A stress drop of 0.2 MPa (top) and 1 MPa (bottom) has been assumed for estimating M_{max}. Two potential failure mechanisms, strike slip or normal faulting, are considered.

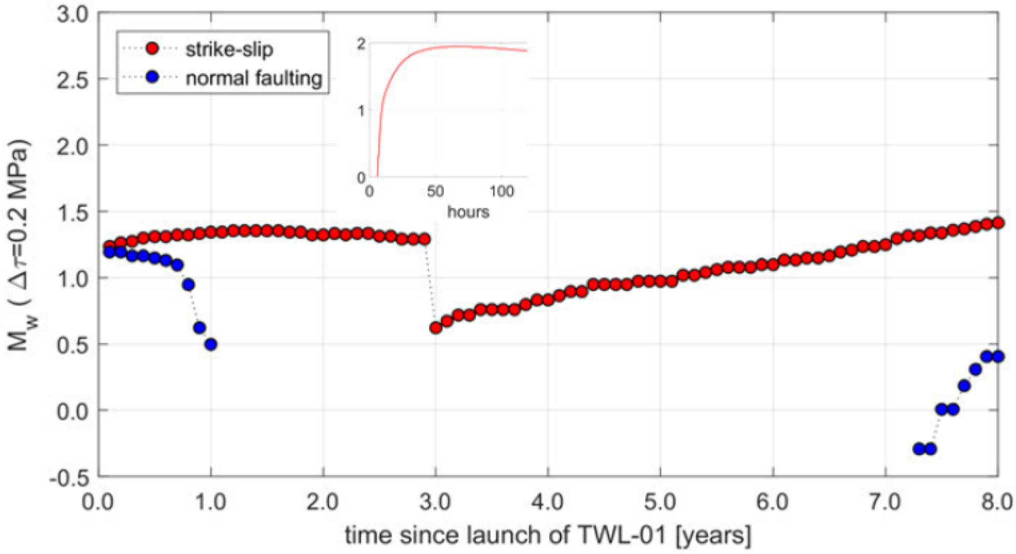

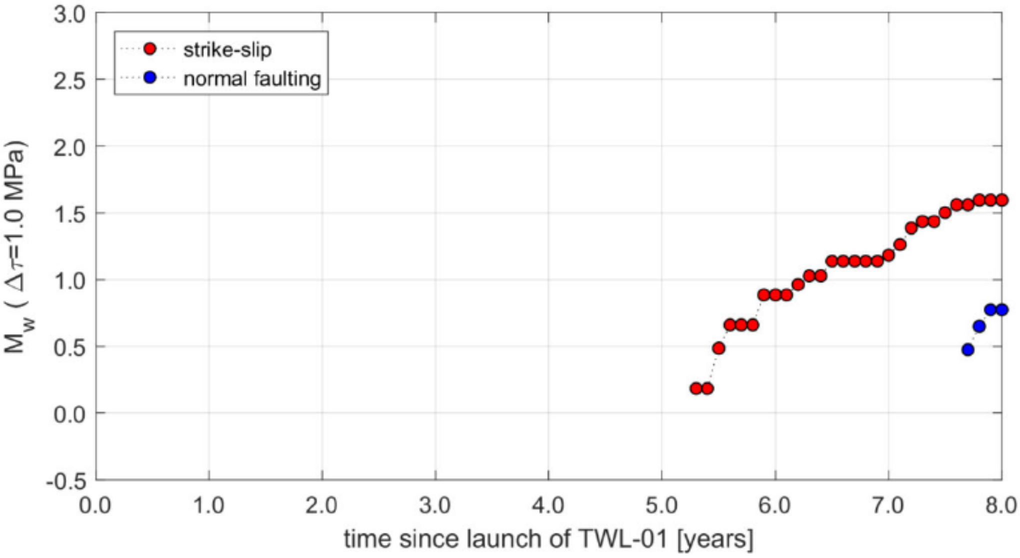

Figure 20: Simulated temporal evolution of maximum earthquake magnitude on fault 7 assuming that the faults react seismically at sedimentary level. A stress drop of 0.2 MPa (top) and 1 MPa (bottom) has been assumed for estimating M_{max}. Two potential failure mechanisms, strike slip or normal faulting, are considered. Small inset in upper panel shows close up of M_{max} evolution during the initial 120 hours (both failure mechanisms exhibit almost identical values). See text for details.

6.4.3 Extreme Scenario: Blind Fault

We consider the hypothetical extreme scenario that one of the injection wells intersects a critically stressed fault. Hydraulic pressure applied to the fault during geothermal production is critically depending on the hydraulic properties of the fault and the surrounding rock, as well as on the hydraulic communication with production wells. An upper limit for the hydraulic overpressure in the fault, however, is given by the theoretical scenario, where all fluid is pumped into the fault (i.e. no matrix leak-off) while the fault does not connect to a production well. This theoretical scenario is investigated in Figure 21 showing hydraulic overpressure after 1, 10 and 30 days of injection. Due to the infinite model extension, the hydraulic pressure does not become (quasi-) stationary and the *in-situ* pressure continuously increases during injection. The velocity at which a certain level of overpressure propagates away from the injection well, however, is largest at the beginning of the injection and decreases with time.

Now consider a critically stressed region of the fault, e.g. located around the center of the model at 3 km depth. This region is subjected to significant overpressure of approx. 1 MPa already after 30 days. The likelihood that the critically stressed fault segments are seismically activated already at an early stage of injection is high. The same line of argumentation holds for any location of a critical stressed patch in the model.

These generic considerations indicate that critically stressed fault patches will be activated already at an early stage of injection. Therefore we recommend operating seismic real-time monitoring and a traffic-light-system as a risk mitigation measure during the initial production phase (chapter 7).

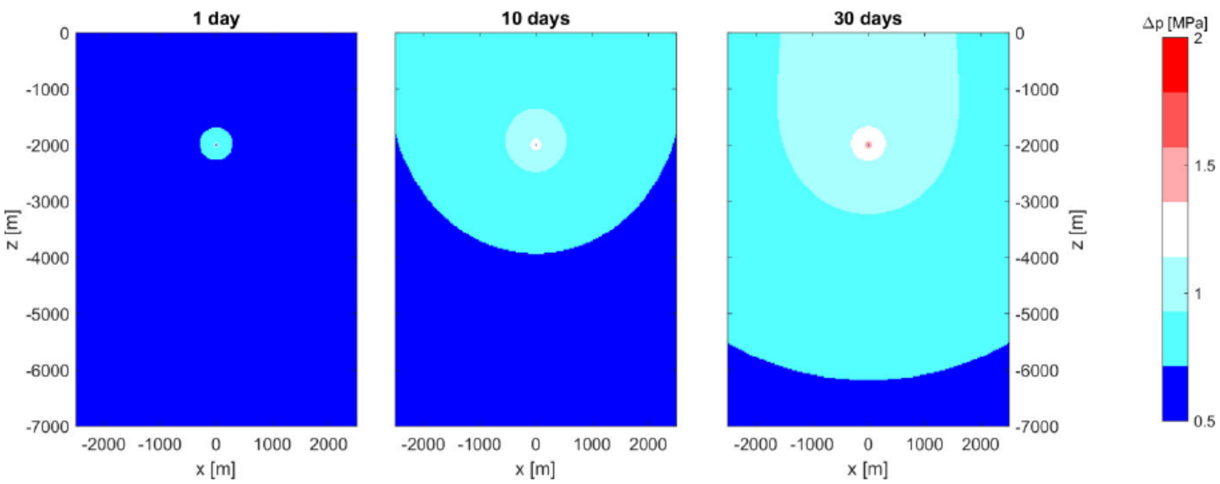

Figure 21: Spatial distribution of hydraulic overpressure for the theoretical scenario of direct injection into a fault with no matrix leak-off. Overpressure were computed with an analytic solution for an infinite reservoir in all directions except for a no-flow boundary at z=0. Fault parameters were chosen in accordance with well-testing observations [2]. Hydraulic pressure in MPa according to the colour map. ***Left****: after 1 day.* ***Centre****: after 10 days.* ***Right****: after 30 days.*

6.4.4 Extreme Scenario: Insufficient Well-Connectivity

If the hydraulic connectivity between injection and production wells is poor[10], geothermal circulation would be associated with mass changes, which could in principle cause seismicity (chapter 4). As long as each geothermal well is hydraulically connected to an (effectively) infinite reservoir, mass changes associated with geothermal production are not relevant in the context of induced seismicity.

This is different for the scenario of a finite reservoir, in which case insufficient well-communication could lead to a systematic pressure increase at an injection well and a pressure drawdown at a production well. In this hypothetical scenario, pressure increase at the injection well would result in a reduced injection rate as the geothermal operations are effectively pressure controlled by the pressure limit (section 5.1). Since seismic hazard is driven by pressure changes rather than rate changes, the impact of injectivity decrease on seismic hazard is considered minor, in particular if pressure monitoring is implemented as a risk mitigation measure and operations are not continued under conditions where the injection pressure significantly increases (compare chapter 7).

It is well known from gas reservoirs that large-scale drawdown of reservoir pressure can lead to reservoir compaction and associated seismicity, e.g. [56,57]. In the scenario depicted above, however, the pressure drawdown is a localized effect near the production well, which is limited in amplitude to approximately 60 bar by the deployment depth of the production pump (section 5.1). Similar to the injection side, the pressure limit would result in a reduced production rate, while pressure drawdown remains a localized phenomenon.

In summary, we conclude that insufficient well-communication does not increase the seismic hazard provided that pressure monitoring is implemented as a risk mitigation measure.

6.5 Shake Maps

In the previous section different hazard scenarios were investigated to estimate a maximum earthquake magnitude that could potentially occur under specific subsurface conditions. To estimate the associated ground vibrations at the Earth's surface, an empirical relationship proposed by Douglas et al. [58] is applied, which provides peak ground velocity (PGV) as a function of earthquake magnitude, distance and hypocentral depth (model 1 in [58]). In a first step, PGV is computed for a hard reference rock without considering near surface amplification factors. Terrain topography is explicitly considered in this step. Subsequently, near surface amplification factors as determined by Poggi et al. [59] are applied. These amplification factors depend on the frequency of the vibration signals and on the shear wave velocity of the near-surface layers.

We performed forward simulations of ground vibrations at 10 Hz assuming that the earthquake hypocenter is located anywhere in a region of positive Coulomb stress changes $\Delta CS > 0.1$ MPa (compare Figure 15 and Figure 16) or at the intersection point of one of the

[10] which is an unlikely scenario for the TWL-01 doublet (Appendix A.3) but cannot be ruled out for the future TWL-02 doublet

injection wells with the reservoir.

Figure 22 shows simulated ground vibrations caused by an M_w=1.3 reservoir earthquake. Our simulation results indicate that this is the magnitude level above which reservoir earthquakes might become perceptible to human beings (PGV=0.5 mm/s).

The magnitude threshold above which reservoir seismicity might cause damage to ordinary buildings is estimated as M_w=2.5 (Figure 23).

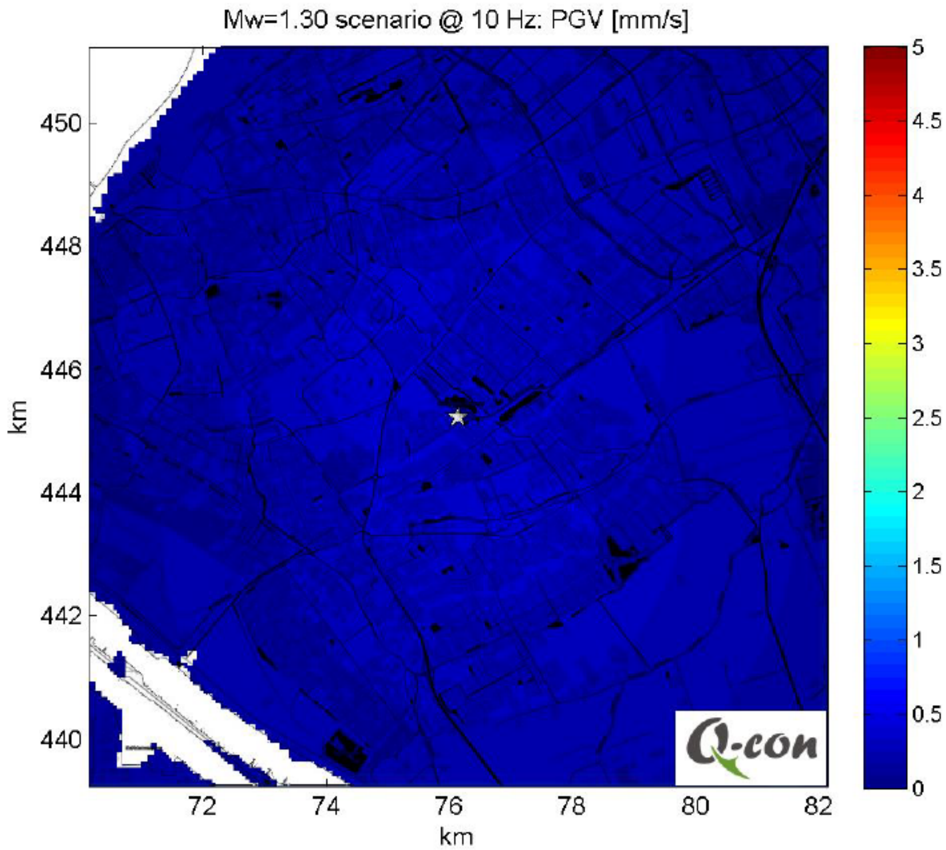

Figure 22: Maximum peak ground velocity for an induced reservoir earthquake of magnitude M_w=1.3. The ground motion velocity is given in mm/s according to the colour scale. The hypocenter is assumed to be located at the intersection point of NLW-GT-01 or NLW-GT-04 with the reservoir or at the point of the highest ΔCS on the two boundary faults. Background map tiles by Stamen Design, under CC BY 3.0. Data by OpenStreetMap, under ODbL.

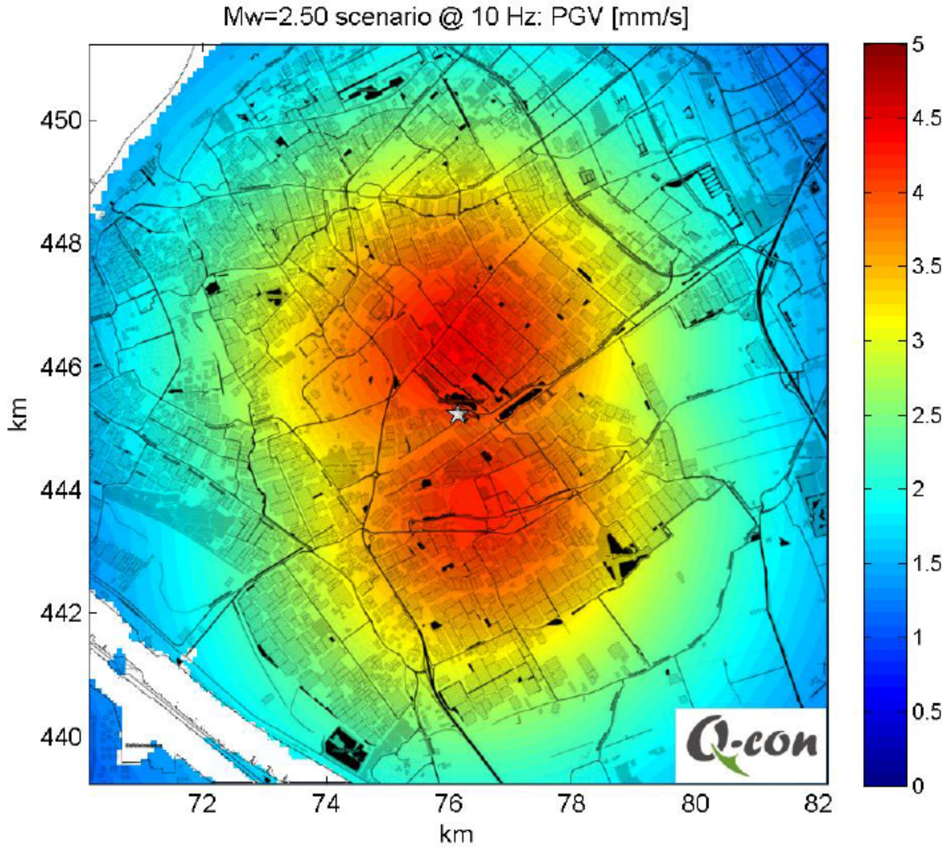

Figure 23: Maximum peak ground velocity for an induced reservoir earthquake of magnitude M_w=2.5. The ground motion velocity is given in mm/s according to the colour scale. The hypocenter is assumed to be located at the intersection point of NLW-GT-01 or NLW-GT-04 with the reservoir or at the point of the highest ΔCS on the two boundary faults. Background map tiles by Stamen Design, under CC BY 3.0. Data by OpenStreetMap, under ODbL.

6.6 Qualitative Risk Assessment

A qualitative seismic risk assessment is performed following the methodology outlined in the recommendations for seismic hazard assessment of geothermal systems in The Netherlands [1].

As discussed above (chapters 3 and 4), induced seismicity is not expected to occur on the known faults due to the rheological behaviour of the sandstone. For the risk assessment we consider the hypothetical case that the boundary faults are critically stressed and respond seismically to stress perturbations. Given the large spatial extension of the fault, the maximum possible earthquake magnitude on the boundary fault is primarily determined by the efficiency of the TLS.

The proposed TLS (chapter 7) is designed to prevent the occurrence of material damage even when accounting for a trailing effect of 1 magnitude units (M_w). Numerical simulations of ground vibrations indicate that the TLS red threshold corresponds to a reservoir earthquake of M_w=1.3 and material damage to ordinary buildings cannot be excluded for M_w>2.5 (section 6.5). We associate an M_w=2.6 reservoir earthquake with moderate consequences following the scheme proposed by [1].

Assuming Gutenberg-Richter statistics (with b=1), the occurrence probability of an M_w=2.6 reservoir earthquake is <10% conditional to the previous occurrence of an M_w=1.3. It should be noted, however, that the absolute occurrence probability of an M_w=2.6 earthquake can be orders of magnitude smaller and cannot be predicted. We qualitatively rank the occurrence probability as unlikely. Figure 24 shows the resulting risk matrix.

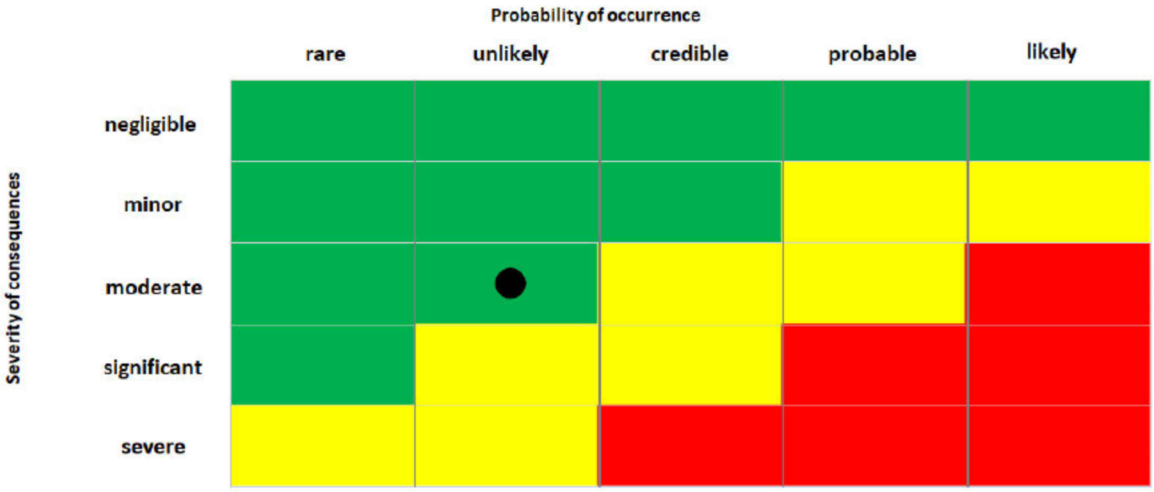

Figure 24: Qualitative risk matrix for the future production scenario of the TWL-01 and TWL-02 doublets with the proposed TLS. See text for details.

7 DEFINITION OF CONTROL AND PROTECTIVE MEASURES

7.1 Traffic Light System

The previous analysis indicates that the seismic hazard associated with the geothermal system at Naaldwijk is low in the ‘expected case scenario’. In the extreme case scenarios considered in the previous chapter, specific subsurface conditions could in principle lead to earthquakes with magnitude M_w>2.5 which could cause (slight) material damage. Therefore, additional control and protective measures are defined.

To avoid the occurrence of damage relevant seismicity, geothermal operations have to be modified or even suspended if induced seismicity above a certain magnitude threshold occurs (‘Traffic Light System’, TLS). This requires continuous seismic monitoring of the geothermal activities.

The monitoring requirements, however, change throughout the lifetime of the geothermal facility. Model simulations in the previous chapter indicate that the rate of stress changes is largest in the early phase of project development, before hydraulic conditions in the subsurface become quasi-stationary. Accordingly, the rate at which the strength of induced seismicity can increase is comparatively high, requiring a small response time in the TLS. At a later stage, requirements are less stringent as stresses change much slower.

The accuracy to which an earthquake of a given magnitude can be prevented by a TLS is limited, in particular due to trailing effects [32]. Therefore, a safety margin is accounted for in the definition of TLS threshold values.

The proposed TLS is summarized in Table 5. During the initial stage of geothermal circulation, the TLS should be operated in real-time. For this, a local detector station with specifications according to Appendix C.2 should be operated in real-time. Fluid circulation should be interrupted (stoplight) if a local earthquake with magnitude M_w≥1.3 occurs (see previous section for further explanation) or if measured ground vibrations at the detector station exceed 0.5 mm/s.

TLS orange is activated if a smaller magnitude earthquake (PGV < 0.5 mm/s and M_w<1.3) is measured at the detector station. In this case, the cause of the earthquake needs to be investigated and reported to the regulator.

Once the system is operated under (quasi-) stationary hydraulic conditions without causing detectable seismicity, less stringent monitoring requirements apply. At this stage, routine monitoring performed by the KNMI in combination with the local (detector) station can be defined as the minimum requirements, operated with a ‘next business day’ response time. Fluid circulation should be interrupted if a local earthquake with magnitude M_w≥1.3 has occurred.

We emphasize that other geothermal facilities and producing hydrocarbon reservoirs exist in close vicinity to the Naaldwjik project. Establishing a causal relationship of a local earthquake to any of these facilities may be complicated or even impossible due to overlapping stress contributions from different facilities. At the same time, hypocenter location uncertainties may prevent a clear discrimination. Therefore we recommend deploying a dedicated seismic monitoring network according to the specifications in C.3 if local seismicity has occurred (i.e. TLS orange).

TLS Status			
Definition	no seismicity	PGV < 0.5 mm/s and Mw < 1.3	PGV ≥ 0.5 mm/s or Mw ≥ 1.3
Actions	none	1. investigate likely cause and potential mitigation measures 2. report to regulator	1. stop operations 2. report immediately to regulator 3. reassess seismic hazard

Table 5: Definition of TLS threshold values. The TLS applies to all earthquakes whose epicenters are located within 5 km to a reference point centered at surface coordinates of GT-01 (76147m / 445237m RK coordinates). Hypocentral depth is not included in the TLS criteria due to its strong dependency on the assumed seismic velocity model. Peak ground velocities (PGV) refer to the seismometer component with the largest amplitude.

7.2 Pressure Monitoring

We recommend to continuously monitor the productivity and injectivity of the geothermal wells. A systematic decrease of the (temperature/density corrected) injectivity or productivity index could be an indicator for insufficient inter-well connectivity (compare extreme scenario in section 6.4.4).

We recommend reviewing the reservoir model and seismic hazard assessment if the averaged injectivity or productivity index has systematically decreased by a factor of ≥2.0 compared to previous values.

8 REMAINING UNCERTAINTIES

The hazard assessment conducted in this study is based on deterministic physical models. These models are consistent with observations of induced seismicity in geothermal systems on a global scale, i.e. previous observations can be sufficiently described by the physics-based models. Using these models, maximum earthquake magnitudes are determined assuming different constellations of subsurface parameters.

Parameter uncertainties are mostly covered by conservative assumptions, where parameters are assumed at the limit of previous observations. Thus, the resulting hazard is deliberately overestimated. Independent of the geomechanical analysis, a Traffic Light System is proposed to limit the maximum strength of potentially induced earthquakes well below the damage level.

In the physics-based analysis it is assumed that the seismic reaction is limited to the region where *in situ* stresses were changed by geothermal operations. Furthermore, it is assumed that a minimum level of $\Delta CS \geq 0.1$ MPa is required for triggering earthquakes. In the following we discuss the implications of these two assumptions.

In theory it is possible that a natural fault exists in the subsurface, which is so close to stress criticality that coseismic stress transfer of an induced earthquake might grow beyond the radius of influence of geothermal stress perturbations [49,60–62]. In this case, a fundamental assumption underlying the current hazard assessment is violated. It is possible that the M_w5.4 Pohang earthquake [27] resulted from this type of scenario. For the specific situation at Naaldwijk, however, such a scenario is considered very unlikely (though not quantifiable) for the following reasons:

- Natural earthquakes are absent in the wider region around Naaldwijk and hydrocarbon production in the South-West of the Netherlands has never been associated with induced seismicity.
- Numerical simulations demonstrate that noticeable Coulomb stress changes associated with geothermal production at Naaldwijk are restricted to the sedimentary section, where the potential for induced seismicity is considered low.
- The absolute level of Coulomb stress changes associated with geothermal production is very small. Much larger Coulomb stress changes were associated with neighboring gas production, which have not caused measurable seismicity.

These aspects indicate that the general stress-state of the local faults is not particularly close to stress criticality, which would be a necessary condition for run-away effects. Furthermore, earthquake triggering at $\Delta CS < 0.1$ MPa appears highly unlikely.

REFERENCES

[1] Baisch S, Koch C, Stang H, Pittens B, Drijver B, Buik N. Defining the Framework for Seismic Hazard Assessment in Geothermal Projects V0.1 - Technical Report. 2016.
[2] de Wijkerslooth C. Winningsplan TWL-01 NLW-GT-01/02. Trias Westland; 2019.
[3] National Research Council. Induced Seismicity Potential in Energy Technologies. Washington, D.C.: The National Academies Press; 2013. doi:10.17226/13355.
[4] Foulger GR, Wilson MP, Gluyas JG, Julian BR, Davies RJ. Global review of human-induced earthquakes. Earth-Science Reviews 2018;178:438–514. doi:10.1016/j.earscirev.2017.07.008.
[5] Healy JH, Hamilton RM, Raleigh CB. Earthquakes induced by fluid injection and explosion. Tectonophysics 1970;9:205–14. doi:10.1016/0040-1951(70)90017-X.
[6] Hsieh PA, Bredehoeft JD. A reservoir analysis of the Denver earthquakes: A case of induced seismicity. J Geophys Res 1981;86:903–20. doi:10.1029/JB086iB02p00903.
[7] Scholz CH. The Mechanics of Earthquakes and Faulting. 2nd ed. Cambridge: Cambridge University Press; 2002. doi:10.1017/CBO9780511818516.
[8] TNO. Literature review on Injection-Related Induced Seismicity and its relevance to Nitrogen Injection. TNO, Earth, Environmental and Life Sciences; 2014.
[9] Evans KF, Zappone A, Kraft T, Deichmann N, Moia F. A survey of the induced seismic responses to fluid injection in geothermal and CO2 reservoirs in Europe. Geothermics 2012;41:30–54. doi:10.1016/j.geothermics.2011.08.002.
[10] Hincks T, Aspinall W, Cooke R, Gernon T. Oklahoma's induced seismicity strongly linked to wastewater injection depth. Science 2018;359:1251–5. doi:10.1126/science.aap7911.
[11] Skoumal RJ, Brudzinski MR, Currie BS. Proximity of Precambrian basement affects the likelihood of induced seismicity in the Appalachian, Illinois, and Williston Basins, central and eastern United States. Geosphere 2018;14:1365–79. doi:10.1130/GES01542.1.
[12] Abdullah RA. A study on stress-strain behaviour of granite and sandstone using closed-circuit servo-controlled testing machine. Master Thesis. Universiti Teknologi Malaysia, 2006.
[13] Hanks TC, Kanamori H. A moment magnitude scale. J Geophys Res 1979;84:2348–50. doi:10.1029/JB084iB05p02348.
[14] Dost B, van Eck T, Haak H. Scaling peak ground acceleration and peak ground velocity recorded in The Netherlands. Bolletino Di Geofisica Teorica Ed Applicata 2004;45:153–68.
[15] Akkar S, Sandıkkaya MA, Bommer JJ. Empirical ground-motion models for point- and extended-source crustal earthquake scenarios in Europe and the Middle East. Bull Earthquake Eng 2014;12:359–87. doi:10.1007/s10518-013-9461-4.
[16] Baria R, Michelet S, Baumgärtner J, Dyer BC, Gerard A, Nicholls J, et al. Microseismic Monitoring of the World's Largest Potential HDR Reservoir. Proceedings 29th Workshop on Geothermal Reservoir Engineering, Stanford University, Stanford, California: 2004, p. 8.
[17] Baisch S, Carbon D, Dannwolf U, Delacou B, Devaux M, Dunand F, et al. Deep Heat Mining Basel - Seismic Risk Analysis. SERIANEX study prepared for the Departement für Wirtschaft, Soziales und Umwelt des Kantons Basel-Stadt, Amt für Umwelt und Energie; 2009.
[18] Baisch S, Rothert E, Stang H, Vörös R, Koch C, McMahon A. Continued Geothermal Reservoir Stimulation Experiments in the Cooper Basin (Australia). Bulletin of the Seismological Society of America 2015;105:198–209. doi:10.1785/0120140208.
[19] Costain JK, Bollinger GA. Review: Research Results in Hydroseismicity from 1987 to 2009. Bulletin of the Seismological Society of America 2010;100:1841–58.

doi:10.1785/0120090288.
[20] Keranen KM, Weingarten M, Abers GA, Bekins BA, Ge S. Sharp increase in central Oklahoma seismicity since 2008 induced by massive wastewater injection. Science 2014;345:448–51. doi:10.1126/science.1255802.
[21] Schoenball M, Walsh FR, Weingarten M, Ellsworth WL. How faults wake up: The Guthrie-Langston, Oklahoma earthquakes. The Leading Edge 2018;37:100–6. doi:10.1190/tle37020100.1.
[22] Husen S, Bachmann C, Giardini D. Locally triggered seismicity in the central Swiss Alps following the large rainfall event of August 2005: Locally triggered seismicity in the central Swiss Alps. Geophysical Journal International 2007;171:1126–34. doi:10.1111/j.1365-246X.2007.03561.x.
[23] Miller SA. Note on rain-triggered earthquakes and their dependence on karst geology. Geophysical Journal International 2008;173:334–8. doi:10.1111/j.1365-246X.2008.03735.x.
[24] Portier S, André L, Vuataz F-D. Review on chemical stimulation techniques in oil industry and applications to geothermal systems 2007:34.
[25] Brown MRM, Ge S. Distinguishing Fluid Flow Path from Pore Pressure Diffusion for Induced Seismicity. Bulletin of the Seismological Society of America 2018;108:3684–6. doi:10.1785/0120180149.
[26] Hubbert MK, Rubey WW. Role of Fluid Pressure in Mechanics of Overthrust Faulting. GSA Bulletin 1959;70:115–206. doi:10.1130/0016-7606(1959)70[115:ROFPIM]2.0.CO;2.
[27] Kim K-H, Ree J-H, Kim Y, Kim S, Kang SY, Seo W. Assessing whether the 2017 Mw5.4 Pohang earthquake in South Korea was an induced event. Science 2018;360:1007–9. doi:10.1126/science.aat6081.
[28] Buness H. GeneSys – Ein Beobachtungsnetz für induzierte seismische Ereignisse. Hannover: Institut für geowissenschaftliche Gemeinschaftsaufgaben (now LIAG); 2004.
[29] Kwiatek G, Bohnhoff M, Dresen G, Schulze A, Schulte T, Zimmermann G, et al. Microseismicity induced during fluid-injection: A case study from the geothermal site at Groß Schönebeck, North German Basin. Acta Geophys 2010;58:995–1020. doi:10.2478/s11600-010-0032-7.
[30] Baisch S, Weidler R, Vörös R, Jung R. A Conceptual Model for Post-Injection Seismicity at Soultz-sous-Forêts 2006:7.
[31] Baisch S, Harjes H-P. A model for fluid-injection-induced seismicity at the KTB, Germany. Geophysical Journal International 2003;152:160–70. doi:10.1046/j.1365-246X.2003.01837.x.
[32] Baisch S, Koch C, Muntendam-Bos A. Traffic Light Systems: To What Extent Can Induced Seismicity Be Controlled? Seismological Research Letters 2019;90:1145–54. doi:10.1785/0220180337.
[33] Bommer JJ, Oates S, Cepeda JM, Lindholm C, Bird J, Torres R, et al. Control of hazard due to seismicity induced by a hot fractured rock geothermal project. Engineering Geology 2006;83:287–306. doi:10.1016/j.enggeo.2005.11.002.
[34] Baisch S, Weidler R, Vörös R, Wyborn D, de Graaf L. Induced Seismicity during the Stimulation of a Geothermal HFR Reservoir in the Cooper Basin, Australia. Bulletin of the Seismological Society of America 2006;96:2242–56. doi:10.1785/0120050255.
[35] Baisch S, Vörös R, Rothert E, Stang H, Jung R, Schellschmidt R. A numerical model for fluid injection induced seismicity at Soultz-sous-Forêts. International Journal of Rock Mechanics and Mining Sciences 2010;47:405–13. doi:10.1016/j.ijrmms.2009.10.001.
[36] Hassanzadegan A, Blöcher G, Zimmermann G, Milsch H, Moeck I. Induced Stress in a Geothermal Doublet System. PROCEEDINGS 2011.
[37] Jeanne P, Rutqvist J, Dobson PF. Influence of injection-induced cooling on deviatoric

stress and shear reactivation of preexisting fractures in Enhanced Geothermal Systems. Geothermics 2017;70:367–75. doi:https://doi.org/10.1016/j.geothermics.2017.08.003.
[38] Bönnemann C, Schmidt B, Ritter J, Gestermann N, Plenefisch T, Wegler U. Das seismische Ereignis bei Landau vom 15. August 2009. 2010.
[39] Küperkoch L, Olbert K, Meier T. Long-Term Monitoring of Induced Seismicity at the Insheim Geothermal Site, Germany. Bulletin of the Seismological Society of America 2018. doi:10.1785/0120170365.
[40] Megies T, Wassermann J. Microseismicity observed at a non-pressure-stimulated geothermal power plant. Geothermics 2014;52:36–49. doi:10.1016/j.geothermics.2014.01.002.
[41] Donselaar ME, Groenenberg R, T Gilding D. Reservoir Geology and Geothermal Potential of the Delft Sandstone Member in the West Netherlands Basin. Proceedings World Geothermal Congress 2015, 2015.
[42] Maaijwee C. Geological report TW OK II. PanTerra Geoconsultants B.V.; 2018.
[43] Wong T, Batjes DAJ, de Jager J, editors. Geology of the Netherlands. Amsterdam, Netherlands: Royal Netherlands Academy of Arts and Sciences; 2007.
[44] Van Adrichem-Boogaert HA, Kouwe W. Stratigraphic nomenclature of the Netherlands; revision and update by RGD and NOGEPA. TNO-NITG, Mededelingen Rijks Geologische Dienst. vol. 50. 1993.
[45] Wassing BBT, Dost B. Seismisch hazard van geïnduceerde aardbevingen - Integratie van deelstudies. TNO/KNMI; 2012.
[46] Heidbach O, Rajabi M, Reiter K, Ziegler M, WSM Team. World Stress Map Database Release 2016 2016. doi:10.5880/wsm.2016.001.
[47] Dost B, W. Haak H. Natural and induced seismicity. In: Wong T, Batjes DAJ, de Jager J, editors. Geology of the Netherlands, Amsterdam, Netherlands: Royal Netherlands Academy of Arts and Sciences; 2007.
[48] Dost B, Kraaijpoel D. The August 16, 2012 earthquake near Huizinge (Groningen) 2013:26.
[49] Buijze L, Bogert PAJ, Wassing BBT, Orlic B. Nucleation and Arrest of Dynamic Rupture Induced by Reservoir Depletion. J Geophys Res Solid Earth 2019;124:3620–45. doi:10.1029/2018JB016941.
[50] Cornell CA. Engineering seismic risk analysis. Bulletin of the Seismological Society of America 1968;58:1583–606.
[51] McGuire RK. Probabilistic seismic hazard analysis and design earthquakes: Closing the loop. Bulletin of the Seismological Society of America 1995;85:1275–84.
[52] Gischig VS, Wiemer S. A stochastic model for induced seismicity based on non-linear pressure diffusion and irreversible permeability enhancement. Geophysical Journal International 2013;194:1229–49. doi:10.1093/gji/ggt164.
[53] Giardini D. Geothermal quake risks must be faced. Nature 2009;462:848–9. doi:10.1038/462848a.
[54] SBR. Schade aan Gebouwen, Deel A uit de Meet– en beoordelingsrichtijn: Trillingen. 2010.
[55] McGarr A. Maximum magnitude earthquakes induced by fluid injection: Limits on fluid injection earthquakes. J Geophys Res Solid Earth 2014;119:1008–19. doi:10.1002/2013JB010597.
[56] Bourne SJ, Oates SJ, van Elk J, Doornhof D. A seismological model for earthquakes induced by fluid extraction from a subsurface reservoir. J Geophys Res Solid Earth 2014;119:8991–9015. doi:10.1002/2014JB011663.
[57] Bourne SJ, Oates SJ, van Elk J. The exponential rise of induced seismicity with increasing stress levels in the Groningen gas field and its implications for controlling seismic risk. Geophysical Journal International 2018;213:1693–700.

doi:10.1093/gji/ggy084.
[58] Douglas J, Edwards B, Convertito V, Sharma N, Tramelli A, Kraaijpoel D, et al. Predicting Ground Motion from Induced Earthquakes in Geothermal Areas. Bulletin of the Seismological Society of America 2013;103:1875–97. doi:10.1785/0120120197.
[59] Poggi V, Edwards B, Fah D. Derivation of a Reference Shear-Wave Velocity Model from Empirical Site Amplification. Bulletin of the Seismological Society of America 2011;101:258–74. doi:10.1785/0120100060.
[60] Galis M, Ampuero JP, Mai PM, Cappa F. Induced seismicity provides insight into why earthquake ruptures stop. Sci Adv 2017;3:eaap7528. doi:10.1126/sciadv.aap7528.
[61] Galis M, Ampuero J-P, Mai PM, Kristek J. Initiation and arrest of earthquake ruptures due to elongated overstressed regions. Geophysical Journal International 2019;217:1783–97. doi:10.1093/gji/ggz086.
[62] Garagash DI, Germanovich LN. Nucleation and arrest of dynamic slip on a pressurized fault: NUCLEATION ON PRESSURIZED FAULT. J Geophys Res 2012;117. doi:10.1029/2012JB009209.
[63] Lingen P. Analysis of Welltest NLW-GT-01. PanTerra Geoconsultants B.V.; 2018.
[64] Lingen P. Interference in NLW-GT-01 of Test NLW-GT-02. PanTerra Geoconsultants B.V.; 2018.
[65] Lingen P. Analysis of Welltest NLW-GT-02. PanTerra Geoconsultants B.V.; 2018.
[66] Okada Y. Internal deformation due to shear and tensile faults in a half-space. Bulletin of the Seismological Society of America 1992;82:1018–40.
[67] Dost B, Goutbeek F, Van Eck T, Kraaijpoel D. Monitoring induced seismicity in the North of the Netherlands: Status report 2010. De Bilt: KNMI; 2012.
[68] Ritter J, Baisch S, Fritschen R, Groos J, Kraft T, Plenefisch T, et al. Empfehlungen zur Überwachung induzierter Seismizität – Positionspapier des FKPE. Mitteilungen Der Deutschen Geophysikalischen Gesellschaft eV 2012;2012/3:17–31.

APPENDIX A WELL TESTING

A.1. Well test GT-01

The test with a duration of 30 hours started on 28-2-2018. The total produced fluid volume from the reservoir was 3350 m^3. Water was produced over 9.5 hours at varying rates followed by a shut-in lasting 21 hours. The production rates varied between 215 m^3/h and 428 m^3/h. Flow rates, pressures and fluid temperatures measured in GT01 are shown in Figure 25. The test has been documented in [63].

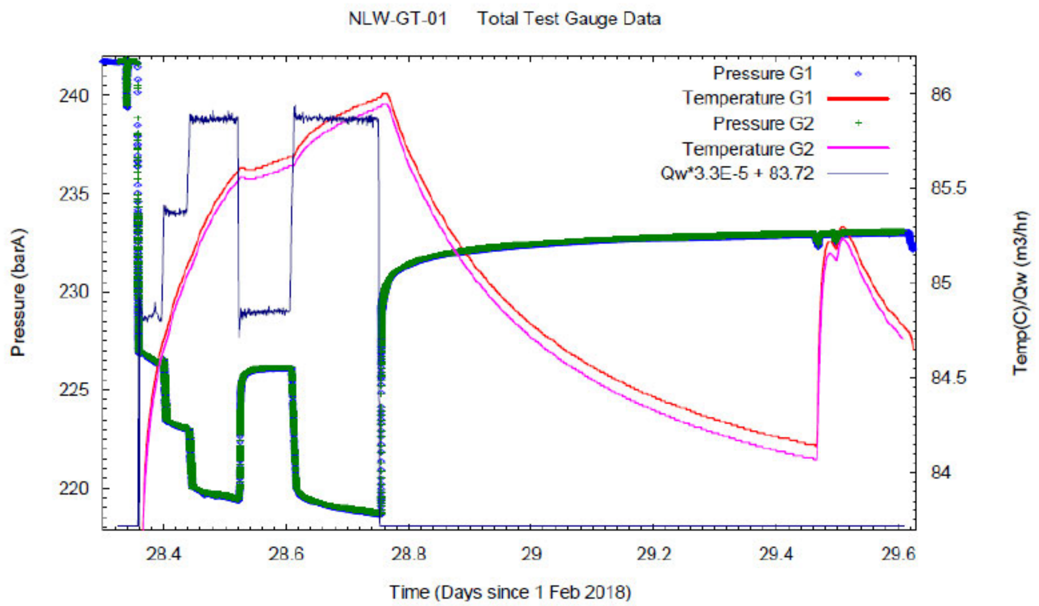

Figure 25: Flow rate, bottom hole pressure and fluid temperature observed during the well testing of GT-01. Figure taken from [63].

A.2. Well test GT-02

Starting on 31-5-2018, the well TGT-02 was tested over 33 hours. The total produced fluid volume from the reservoir was 2980 m^3. The fluid was produced over 9.5 hours at varying rates between 223 m^3/h up to 450 m^3/h. The production was followed by a shut in lasting 23.5 hours (Figure 26). At the same time, pressure in the GT-01 well was monitored (interference test) to assess the communication between the two wells and to obtain a better estimate of global reservoir parameters (Figure 27). It was qualitatively concluded that an excellent communication exists between the wells GT-01 and GT-02 [64].

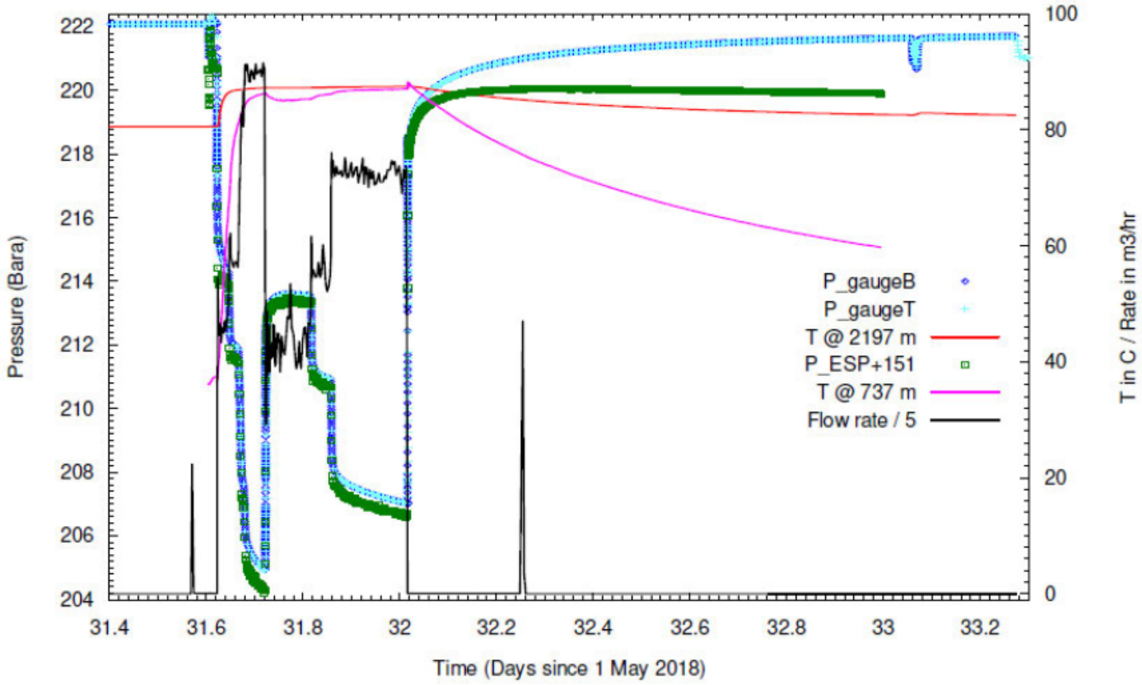

Figure 26: Observed flow rate, downhole pressure and fluid temperature at the GT-02 well during the test. Figure taken from [65].

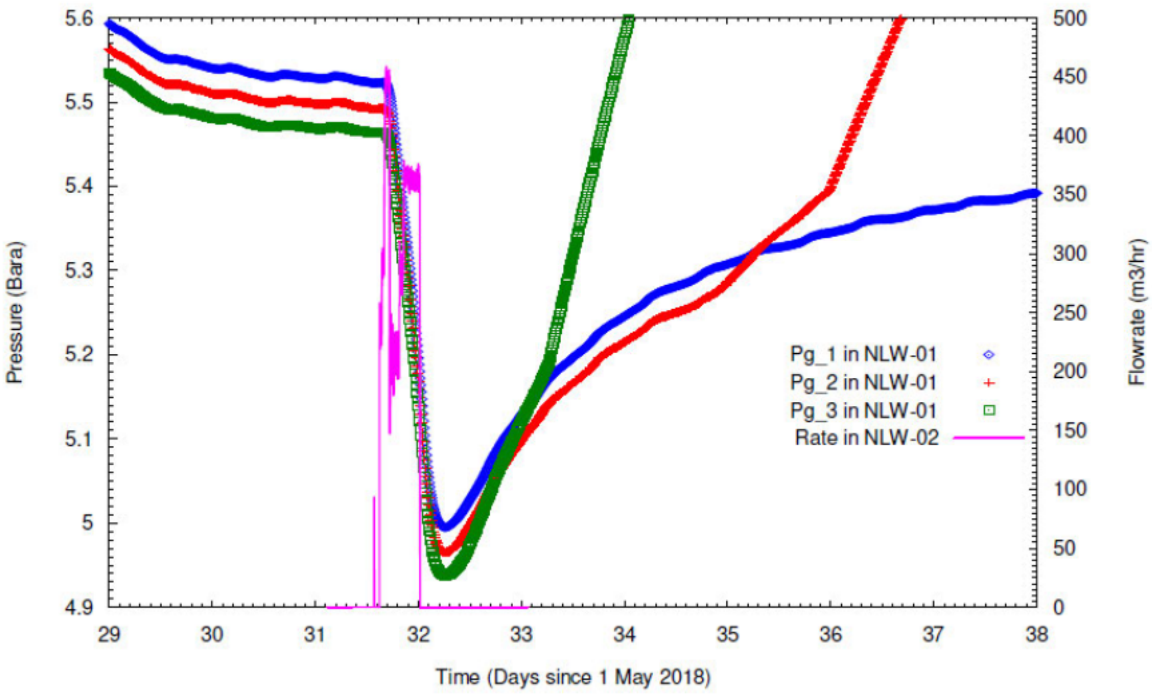

Figure 27: Observed/calculated pressure at 3 different gauges at GT-01 during the testing of GT02. Figure taken from [64].

A.3. Circulation test

Since 15-7-2019, fluid is circulated between the wells GT-01 (injection) and GT-02 (production). The flow rate is approximately 200 m^3/h including short time windows with an increased flow rate of up to 350 m^3/h. Injection pressure was in the order of 40 bar at the beginning of the circulation test and decreased to the level of 30 bar after 6 days at the same injection rate (Figure 28). During high rate injection, the pressure exceeded 50 bar for a short period of time.

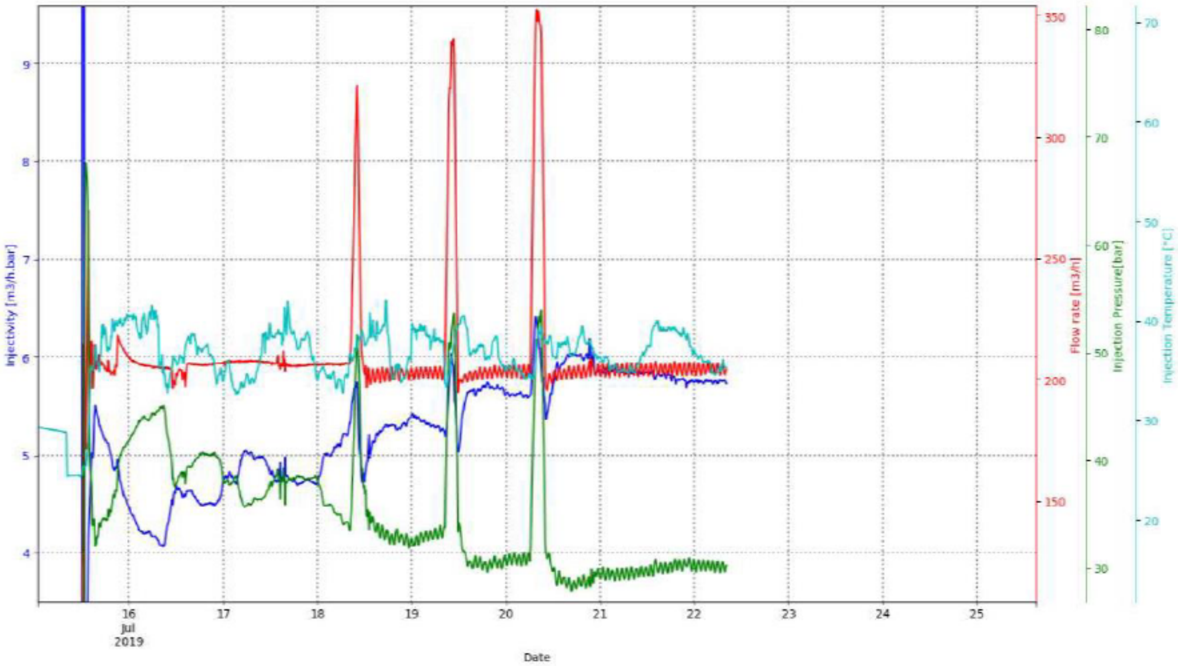

Figure 28: Flow rate (red), injection pressure (green) and fluid temperature (light blue) at GT-01 during the first approximately 6 days of the circulation test. The dark blue curve shows the injectivity index which is systematically increasing in the course of the circulation test. Figure provided by C. Wijkerslooth (HVC).

APPENDIX B NUMERICAL MODEL

The numerical model is based on data and interpretations provided by HVC. Faults, layer surfaces and wellbore trajectories were provided in digital form (E-mail T. Hopmann, HVC, 24-6-2019).

B.1. Hydraulic model

The hydraulic model consists of the reservoir layer and the boundary faults (#1 and #2 in Figure 6) enclosing the central reservoir block in the NW-SE direction. It is not clear if the smaller faults (#3 and #7 in Figure 6) are true structures. Well testing provided no indications for the existence of these structures. Therefore, the smaller faults were not explicitly implemented in the hydraulic model. We note, however, that the modelling results are not sensitive to the hydraulic properties of the smaller faults. The model extension is 8,000 m parallel to the boundary faults (NW-SE) and 5,000 m in the orthogonal direction. Figure 29 shows the reservoir geometry.

The reservoir layer is assumed to be hydraulically isolated against the over- and underburden (clay deposits at the top and bottom). Fault throw at the boundary fault is up to 200 m, resulting in partly detached and partly overlapping segments of the reservoir layer on both sides of the faults. The fault thickness is assumed with 50 m.

Wellbores are implemented as line sources in the central reservoir block within the reservoir layer. All simulations are performed with the planned production pattern depicted in *Figure 4*. Numerical simulations are conducted with the COMSOL Finite-Element software package. The finite-element mesh of the model is shown in Figure 30. The mesh resolution is increased at the wellbores and on the faults. Darcian flow is simulated with no-flow conditions at the outer model boundaries except for the NW-model boundary, where constant pressure conditions have been set according to the HVC interpretation. Based on the results of the well tests (see section 5.4), the reservoir layer is assigned an anisotropic permeability distribution with increased values in the direction parallel to the bounding faults. Fault permeability is assumed to be the same as in the reservoir. Table 6 lists the hydraulic model parameters.

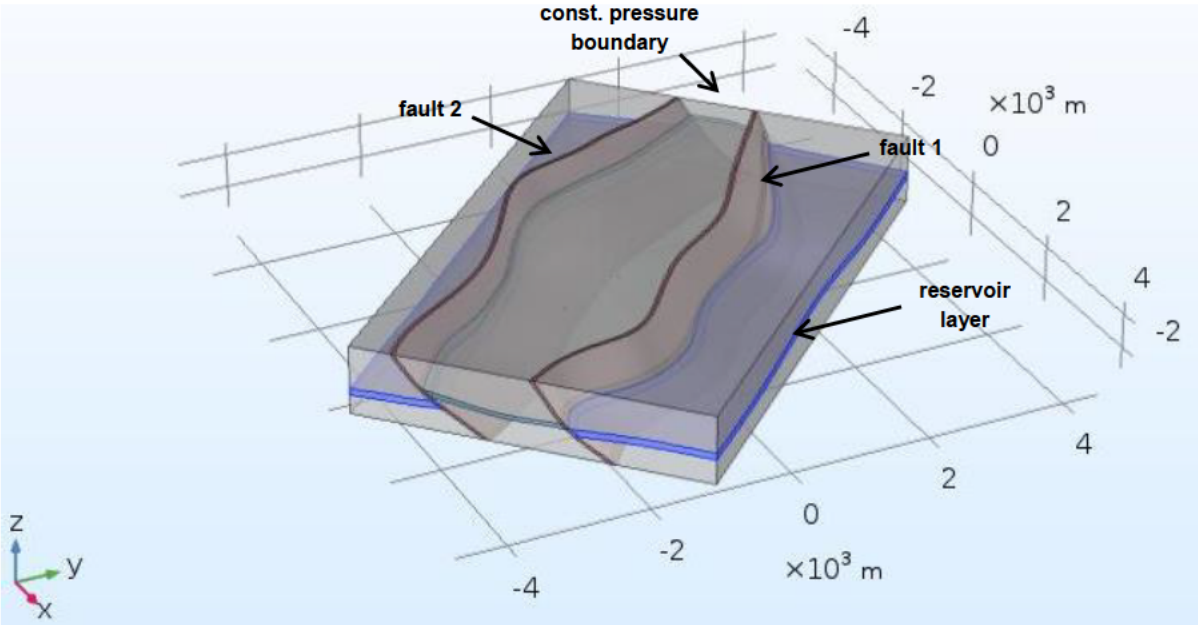

Figure 29: Geometry of the hydraulic model. The model consists of the reservoir layer (blue), the boundary faults (red) and the over- and underburden. Over- and underburden are implemented but not active for the simulation (see text for details). Y-axis points in Northern direction.

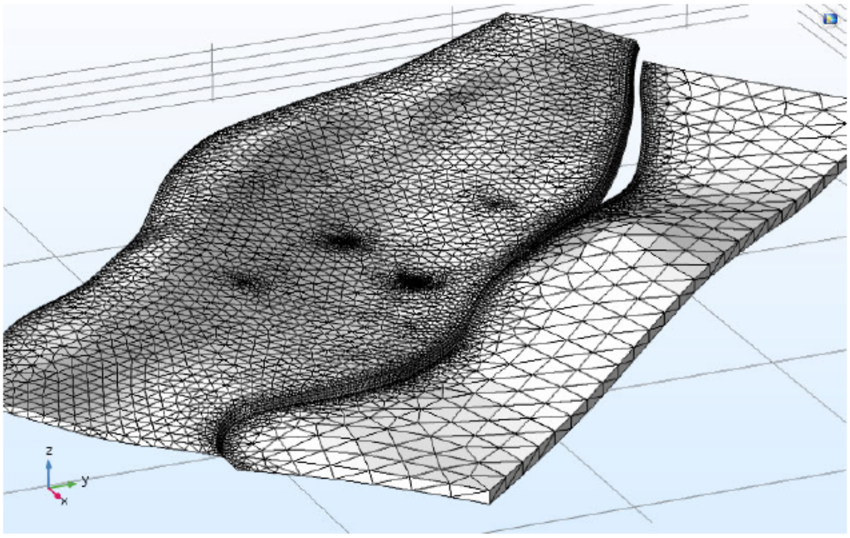

Figure 30: Finite-Element mesh of the hydraulic model. The mesh exhibits an increased resolution at the wellbores in the central reservoir block and at the boundary faults.

Type	Parameter	Value
fluid / rock	dynamic viscosity	0.433 cP
	total compressibility	3.6e-6 psi^{-1}
reservoir rock	permeability	1550 mD (NW/SE) 410 mD (SW/NE) 800 mD (isotropic)
	porosity	18.7%
operational	flow rate	430 m^3/h (TWL-01) 300 m^3/h (TWL-02) pattern according to *Figure 4*

Table 6: Parameter of the hydraulic model.

B.2. Geomechanical Model

Semi-analytical solutions are utilized for simulating thermo-mechanical stresses on the mapped faults following the approach described in [17]. The rock contraction related to the cooling front around the wellbores is approximated by sets of three mutually orthogonal Okada sources [66] as depicted in Figure 31. The rectangular sources represent a volumetric cube in which the reservoir rock has contracted. The overall extension of the cube reflects the thermal energy that has been extracted from the reservoir at a specific time while assuming a constant temperature decline inside the cube. The cubes extend vertically over the reservoir depth interval, slightly exceeding the depth range by 10% in both directions to take into account the partial cooling of the over- and underburden. As a limitation of the semi-analytical approach, thermo-mechanical stresses can only be simulated at those fault locations which are not intersected by the Okada sources.

Type	Parameter	Value
reservoir rock	density	2500 kg/m^3
	Young's modulus	20 GPa
	Poisson's ratio	0.25
	coefficient of internal friction	0.6
	linear coefficient of thermal expansion	1.08e-5
	reservoir temperature	87°C-87.5°C
	specific heat	2268 $kJ/m^3/K$
fluid	re-injection temperature	35°C
	specific heat	4180 J/kg/K
	density	1050 kg/m^3
stress field	orientation S_H	335°

Table 7: Parameter used for the geomechanical simulations..

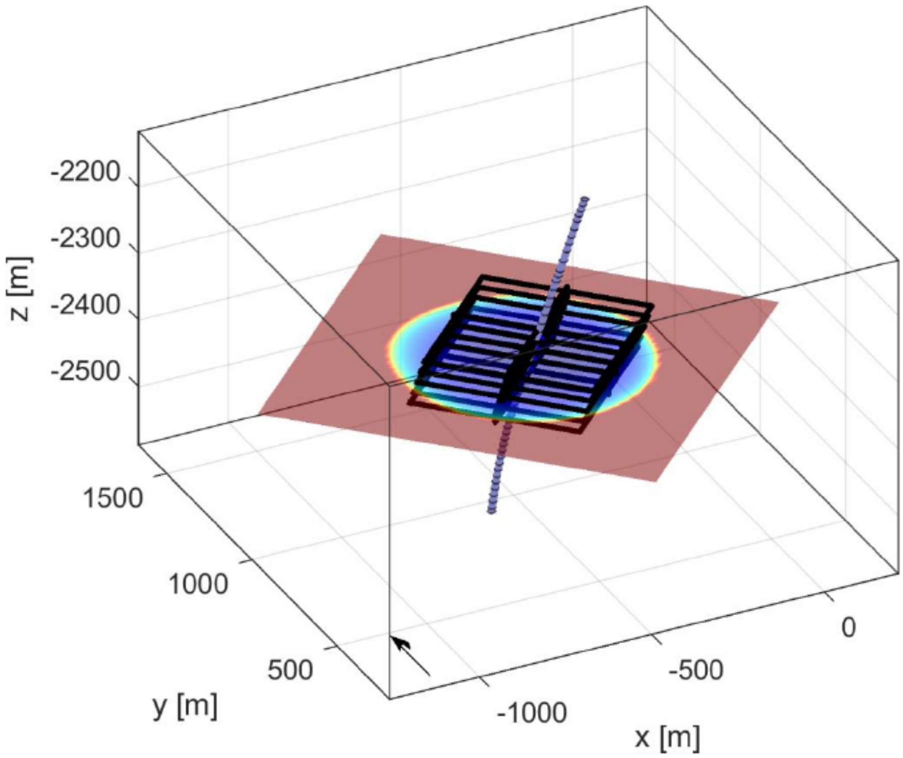

Figure 31: Schematic showing the thermal cooling around the injection well (blue colors) and the approximation of the cooled volume (defined by the ΔT=50°C isosurface) with a set of 36 Okada sources (open rectangles).

APPENDIX C : SEISMIC MONITORING

C.1. KNMI Monitoring Network

Earthquake activity in the Netherlands is monitored by the KNMI, e.g. [67]. The capability for detecting earthquakes with the KNMI seismic monitoring network varies over the Netherlands and has changed over time as new monitoring stations were deployed. For the current study it is important to evaluate today's monitoring capabilities of the KNMI network for earthquakes occurring near the Naaldwijk geothermal location.

The lower magnitude detection threshold for the seismic monitoring network in its configuration of the year 2010 is shown in [67]. The magnitude detection limit for other configurations of the KNMI seismic monitoring network, however, is not published in the scientific literature. We use results of [67] for calibrating our own numerical simulation of the lower magnitude detection limit. We use the same formula as [67] for relating magnitude to ground motion. For the 2010 network configuration, our simulation results are almost identical to those published by [67].

Figure 32 shows the simulated lower magnitude detection threshold for the KNMI network as of 2019. The theoretical detection threshold near Naaldwijk is at approx. M_L=0.5. It is, however, not clear if the routine processing at KNMI would actually detect earthquakes at this magnitude level.

Given the sparse station density in the South West of The Netherlands, the capability of locating earthquakes in the Naaldwijk region is limited. Even for a moderate sized earthquake of M_L=1.5, epicenter location errors might be at the 10 km level.

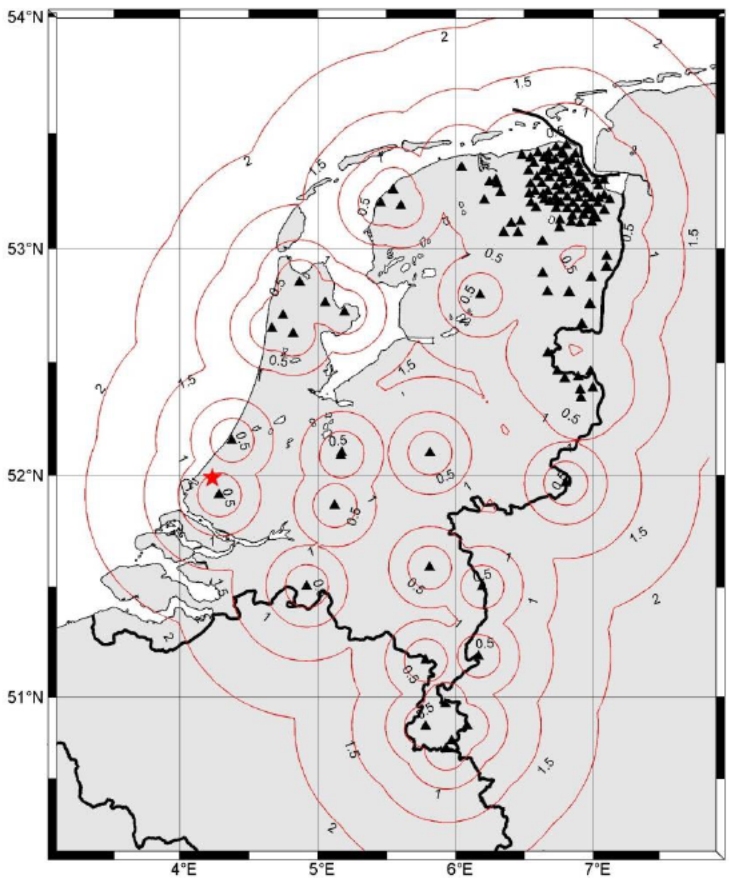

Figure 32: Simulated lower magnitude detection threshold (M_L) for the KNMI seismic station network as of 2019 (assuming all stations are operating). The locations of the seismic stations are indicated by black triangles, the geothermal project site by a red star. Event depth is assumed at 2.5 km. Data source: The Royal Netherlands Meteorological Institute: Overzicht van Nederlandse stations. https://knmi.nl/nederland-nu/seismologie/stations, accessed on 15.07.2019.

C.2. Detector Station

Monitoring with a single detector station should provide basic data for an analysis, e.g. in case a felt earthquake is reported by the local population. The occurrence of the earthquake could then be confirmed by the instrument recordings, although only an approximate earthquake location can be estimated from single station recordings. In case an earthquake is detected that could potentially be associated with the geothermal system, it is recommended to (temporarily) deploy a more comprehensive monitoring network as outlined in section C.3.

The existing KNMI station ZH01 at Vlaardingen could in principle serve as the detector station. The station, however, is located approx. 9.5 km away from the geothermal site. To improve the lower detection limit in the early production phase we recommend operating an additional monitoring station located ≤ 2 km from the Naaldwijk geothermal site with the following specifications:

- Short-period, 3 component seismometer.
- 24bit acquisition system.
- GPS synchronization.
- Sampling at 100 Hz.
- Real-time data streaming.
- Data format compatible with KNMI recordings.

C.3. Local Monitoring Network

The current seismic hazard assessment yields a low potential for inducing seismicity by the planned geothermal production. Therefore, operation of a dedicated local monitoring network is not required.

If, however, seismicity of unknown origin is detected in the Naaldwijk region, data from local seismic monitoring stations might be required to investigate a potential relationship to geothermal activities. In this case, (temporal) operation of a 5 station network is recommended following the specifications of [68]:

- A minimum number of 5 monitoring stations should be operated. An optimized station geometry depends on the number of stations included in the network and can be modelled as part of the network design. The 2σ hypocenter location accuracy for seismicity occurring in or near the geothermal reservoir should be at least +/- 500 m in horizontal, and +/- 2000 m in the vertical direction, respectively
- The location of the stations should exhibit a comparatively low level of background noise. The detection threshold for reservoir earthquakes should be in the range between M_L=0 and M_L=1.
- To facilitate the detection of secondary seismic waves, 3-component seismometers should be used.
- The eigenfrequency of the seismometers should be ≤1 Hz.
- The instrumental registration should be based upon an absolute time base (GPS synchronization). The sampling frequency should be at least 100 Hz.
- Data should be recorded time continuously on a 24bit acquisition system.
- Real-time data access is required.
- A standard seismological data format should be used.